CrossMark

ARTICLE

Platinum-group element concentrations in pyrite from the Main Sulfide Zone of the Great Dyke of Zimbabwe

R. Piña[1] · F. Gervilla[2] · S.-J. Barnes[3] · T. Oberthür[4] · R. Lunar[1,5]

Abstract The Main Sulfide Zone (MSZ) of the Great Dyke of Zimbabwe hosts the world's second largest resource of platinum-group elements (PGE) after the Bushveld Complex in South Africa. The sulfide assemblage of the MSZ comprises pyrrhotite, pentlandite, chalcopyrite, and minor pyrite. Recently, several studies have observed in a number of Ni-Cu-PGE ore deposits that pyrite may host significant amounts of PGE, particularly Pt and Rh. In this study, we have determined PGE and other trace element contents in pyrite from the Hartley, Ngezi, Unki, and Mimosa mines of the Great Dyke by laser ablation inductively coupled plasma mass spectrometry (LA-ICP-MS). Based on the textures and PGE contents, two types of pyrite can be differentiated. Py1 occurs as individual euhedral or subhedral grains or clusters of crystals mostly within chalcopyrite and pentlandite, in some cases in the form of symplectitic intergrowths, and is PGE rich (up to 99 ppm Pt and 61 ppm Rh; 1.7 to 47.1 ppm Ru, 0.1 to 7.8 ppm Os, and 1.2 to 20.2 ppm Ir). Py2 occurs as small individual euhedral or subhedral crystals within pyrrhotite, pentlandite, and less frequently within chalcopyrite and silicates and has low PGE contents (<0.11 ppm Pt, <0.34 ppm Rh, <2.5 ppm Ru, <0.37 ppm Ir, and <0.40 ppm Os). Py1 contains higher Os, Ir, Ru, Rh, and Pt contents than the associated pyrrhotite, pentlandite, and chalcopyrite, whereas Py2 has similar PGE contents as coexisting pyrrhotite and pentlandite. Based on the textural relationships, two different origins are attributed for each pyrite type. Py1 intergrowth with pentlandite and chalcopyrite is inferred to have formed by late, low temperature (<300 °C) decomposition of residual Ni-rich monosulfide solid solution, whereas Py2 is suggested to have formed by replacement of pyrrhotite and pentlandite caused by late magmatic/hydrothermal fluids.

Keywords Pyrite · Base metal sulfides · PGE · LA-ICP-MS · Main sulfide zone · Great Dyke · Zimbabwe

✉ R. Piña
  rpinagar@ucm.es

1 Dpto. Cristalografía y Mineralogía, Fac. Ciencias Geológicas, Universidad Complutense de Madrid, Madrid, Spain

2 Dpto. Mineralogía y Petrología and Instituto Andaluz de Ciencias de la Tierra, Fac. Ciencias, Universidad de Granada-CSIC, Granada, Spain

3 Sciences de la Terre, Université du Québec à Chicoutimi, Chicoutimi, Canada

4 German Federal Institute for Geosciences and Natural Resources (BGR), Hannover, Germany

5 Instituto de Geociencias IGEO (UCM-CSIC), Madrid, Spain

Introduction

Pyrite [FeS_2] is a common minor sulfide in Ni-Cu-platinum-group element (PGE: Os, Ir, Ru, Rh, Pt, and Pd) magmatic sulfide deposits where the ore mineralogy usually consists of variable amounts of pyrrhotite [$(Fe_{1-x})S$], pentlandite [$(Fe, Ni)_9S_8$], and chalcopyrite [$CuFeS_2$]. This base metal sulfide assemblage forms by exsolution of pyrrhotite and pentlandite from monosulfide solid solution (MSS) and exsolution of chalcopyrite and pentlandite from intermediate solid solution (ISS) (e.g., Naldrett 2004; Barnes and Ligthfoot 2005). The MSS and ISS crystallized from magmatic sulfide liquid which segregated by liquid immiscibility from ultramafic-mafic silicate magmas at magmatic temperatures after reaching sulfide saturation. However, the origin of pyrite in the sulfide assemblage is not well constrained. Experimental studies show that

pyrite may form by exsolution from MSS at temperatures below 700 °C if the ore composition falls on the S-rich side of MSS in the ternary system Fe-Ni-S (Naldrett et al. 1967; Kullerud et al. 1969; Craig 1973). However, this process does not seem to be very common because most natural sulfide melts do not contain the required amount of sulfur (around 40 wt% S at 600 °C, Kullerud et al. 1969; Craig 1973). Alternatively, it has been proposed that pyrite forms as a result of partial to total replacement of pre-existing sulfides (mainly pyrrhotite) due to the activity of late magmatic, hydrothermal, and/or metamorphic fluids (e.g., Djon and Barnes 2012; Piña et al. 2013; Smith et al. 2011; Holwell et al. 2014; Vukmanovic et al. 2014). The renewed interest in understanding the origin of pyrite follows the discovery that pyrite can contain significant amounts of PGE, particularly Rh, Ru, Os, Ir, and Pt, most probably in solid solution (e.g., Oberthür et al. 1997; Dare et al. 2011; Djon and Barnes 2012; Piña et al. 2013; Smith et al. 2014; Duran et al. 2015). The concentration levels of PGE in pyrite appear to be linked to its origin. In general, pyrite replacing pre-existing sulfides (mainly pyrrhotite, less commonly pentlandite) inherits the concentrations of Os, Ir, Ru, and Rh of the replaced mineral (Dare et al. 2011; Djon and Barnes 2012; Piña et al. 2013; Smith et al. 2014; Duran et al. 2015). In contrast, pyrite directly precipitated from hydrothermal or metamorphic fluids is poor in IPGE (Os + Ir + Ru) relative to pyrrhotite and pentlandite (Piña et al. 2013). Furthermore, the detection of trace amounts of Pt in pyrite is significant, as Pt concentrations in pyrrhotite, pentlandite, and chalcopyrite are very low and Pt is typically present in the form of discrete platinum-group minerals (PGM) in most Ni-Cu-PGE deposits (e.g., Ballhaus and Sylvester 2000; Barnes et al. 2006; Godel and Barnes 2008). It is, thus, important to understand the formation mechanisms of pyrite in Ni-Cu-PGE ores to determine its impact on the distribution of PGE in the deposits.

In the Great Dyke of Zimbabwe, the world's second largest resource of PGE after the Bushveld Complex in South Africa (Naldrett 2011; Zientek 2012), pyrite forms part of the base metal sulfide assemblage consisting of pyrrhotite (~40–50 vol% total sulfides) and approximately equal amounts (~25–30 vol%) of pentlandite and chalcopyrite (Oberthür 2011). Whereas pyrite in most Ni-Cu sulfide mineralization occurs exclusively associated with pyrrhotite (e.g., Dare et al. 2011; Piña et al. 2013; Duran et al. 2015), in the Great Dyke pyrite, in addition to being related to pyrrhotite, also exhibits unusual textures consisting of small individual grains intimately intergrowth in a symplectitic manner with pentlandite and chalcopyrite. In this contribution, we have determined the concentrations of PGE, Au, Ag, Co, Se, As, Te, Bi, and Sb of pyrite from the Hartley, Ngezi, Unki, and Mimosa mines (Fig. 1) which exploit the Main Sulfide Zone (MSZ) of the Great Dyke of Zimbabwe, using laser ablation inductively coupled plasma mass spectrometry (LA-ICP-MS). In addition

to assessing the role of pyrite as host of PGE, we use the trace element concentrations and the textures exhibited by pyrite to discuss the possible mechanisms involved in its formation.

The Great Dyke of Zimbabwe

The Great Dyke of Zimbabwe (Fig. 1) is a 550-km long and 4- to 11-km wide linear, mafic, and ultramafic layered intrusion that was emplaced into Archean granites and greenstone belts of the Zimbabwe craton at 2575 ± 0.7 Ma (Oberthür et al. 2002). On the basis of structure and style and continuity of layering, the Great Dyke is subdivided into several contiguous magmatic chambers and subchambers (Prendergast 1987; Wilson and Prendergast 1989; Wilson 1998): the Musengezi, Darwendale, and Sebakwe subchambers of the North Chamber, and the Selukwe and Wedza subchambers of the South Chamber (Fig. 1). The Great Dyke shows a well-defined igneous stratigraphy and is divided into a lower Ultramafic Sequence (dunite, harzburgite and pyroxenite) and an upper Mafic Sequence (gabbro and norite) (Wilson 1982; Wilson and Prendergast 1989). In the North chamber, the Ultramafic Sequence is characterized by relatively few, thick (avg 100 m) cyclic units, whereas in the South chamber, it has a greater number of thinner (10–30-m thick) cyclic units. The economic PGE mineralization (3–5 ppm of Pt + Pd + Rh + Au, Oberthür 2011) is restricted to disseminations of intercumulus sulfides (up to 10 modal %) in the several meters-thick MSZ situated in pyroxenites some meters below the transition from the Ultramafic to the Mafic Sequence (Prendergast and Wilson 1989; Oberthür et al. 1997; Wilson and Prendergast 2001; Oberthür 2011). The MSZ is a laterally continuous layer, and its stratigraphic position is remarkably persistent in all subchambers. From the base upward, the MSZ displays a well-defined metal zonation characterized by a number of consecutive peaks of PGE, base metals and sulfide (Fig. 2) (e.g., Prendergast and Wilson 1989; Oberthür 2002, 2011). The MSZ is divided into a basal PGE subzone which overlaps slightly with an overlying base metal sulfide (BMS) subzone. The PGE subzone is further divided into a lower part (Pd > Pt) and an upper part (Pd < Pt) (Fig. 2). Upward within the MSZ, Pd/Pt and IPGE/PPGE ratios decrease (IPGE = Os + Ir + Ru; PPGE = Rh + Pd + Pt). The peak of Pt marks the transition from the PGE to BMS subzones (Fig. 2). The upward zoning sequence Pd → Pt → base metal sulfides is interpreted to be a primary magmatic feature consisting in decoupling of Pd from Pt and the PGE group of a whole from the base metals by a combined equilibrium-Rayleigh fractionation (Wilson and Tredoux 1990; Wilson 2001). The most strongly chalcophile elements were preferentially concentrated in the first sulfide liquid and became rapidly depleted in the residual liquid and subsequently formed sulfide. Alternatively, Boudreau and Meurer (1999) suggest that the zoning trends

Fig. 1 Generalized geology and subdivision into chambers and subchambers of the Great Dyke (after Wilson and Prendergast 1989; Wilson 1998). Also shown are the localities of platinum mines studied
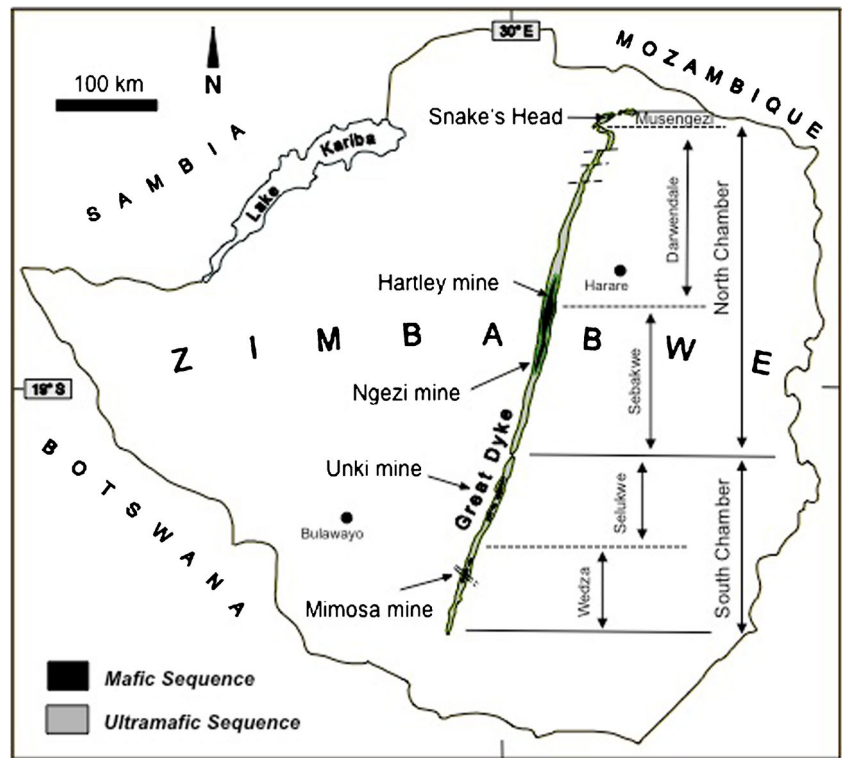
of the MSZ result from a chromatographic control during upward migration of aqueous fluids. According to this model, the metal fractionation could have developed in a vapor-refining zone as fluids evolved during solidification of a cumulus pile, leached sulfide and deposited it higher up in the crystal pile. The metal patterns are proposed to result from different chemical velocities of the various PGE in an upward migrating zone.

In the MSZ, sulfides mainly comprise, in decreasing order of abundance, pyrrhotite, pentlandite, chalcopyrite, and subordinate pyrite. Mackinawite, violarite, galena, sphalerite,

Fig. 2 Schematic showing the metal zonation of the Main Sulfide Zone (after Oberthür 2011)

rutile, molybdenite, cobaltite, argento-pentlandite, and various PGM (moncheite, maslovite, merenskyite, michenerite, sperrylite, and cooperite-braggite) are rare constituents (Oberthür et al. 2003). Detailed reviews of the geology, petrography, and mineralization of the Great Dyke were provided by Wilson (2001), Prendergast (1998), Wilson and Prendergast (2001), and Oberthür (2002, 2011).

Sampling and analytical methods

A total of eight representative samples of the MSZ (two from the Hartley mine, two from Ngezi mine, three from Unki mine, and one from Mimosa mine) were selected on the basis of their relatively high modal abundances of pyrite. Pyrite is common in the BMS subzone of the MSZ but it is particularly abundant at and around the Pt-peak situated at the top of the PGE subzone. Accordingly, the studied samples were selected from the Pt-peak section of the MSZ in the four mines. In order to compare the trace element concentrations between pyrite and coexisting base metal sulfides, we also analysed pyrrhotite, pentlandite, and chalcopyrite where these sulfides are also present in a same aggregate. Pyrrhotite, pentlandite, chalcopyrite, and pyrite grains were studied using reflected-light optical microscopy and selected for laser ablation analyses in 2.5-cm diameter polished blocks. Sulfides were first analysed for major elements (S, Fe, Ni, and Cu) at the Electron Microscope Centre of the University Complutense
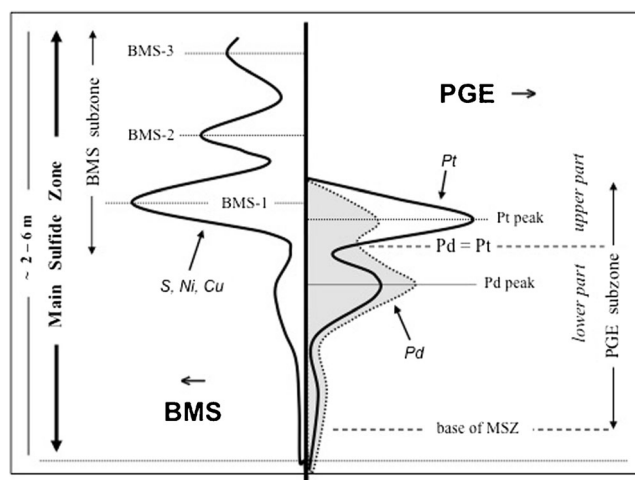
of Madrid, using a JEOL JXA-9800 M electron microprobe. The accelerating voltage was 20 kv, the beam current 50 nA, and the beam diameter 1 to 5 μm. Galena (PbS) for S and pure metals for Ni, Fe, and Cu were used as standards.

The trace elements were determined by LA-ICP-MS at LabMaTer, Université du Quebec à Chicoutimi (UQAC), Canada, using a Resolution 193-nm Excimer laser with a M-50 ablation cell and an Agilent 7700× quadrupole mass spectrometer. An argon-helium gas mix was used as carrier gas. Samples and reference materials were placed in the chamber together, and the reference materials were run before and after each sample. The spectra were collected for 30 s with the laser switched off to determine the base line. Then, line scans across the grains were carried out using a beam size of 33 μm, a laser frequency of 15 Hz, a power of 0.5 mJ/cm^3, and a speed of lateral laser displacement of 5 μm/s. The material was then analysed using the mass spectrometer in time resolution mode using mass jumping and a dwell time of 10 ms/peak. The following isotopes were monitored: ^{29}Si, ^{33}S, ^{34}S, ^{57}Fe, ^{59}Co, ^{60}Ni, ^{61}Ni, ^{63}Cu, ^{65}Cu, ^{66}Zn, ^{75}As, ^{82}Se, ^{99}Ru, ^{101}Ru, ^{103}Rh, ^{105}Pd, ^{106}Pd, ^{107}Ag, ^{108}Pd, ^{111}Cd, ^{121}Sb, ^{125}Te, ^{187}Re, ^{189}Os, ^{191}Ir, ^{193}Ir, ^{195}Pt, ^{197}Au, ^{206}Pb, ^{208}Pb, and ^{209}Bi. Data reduction was carried out using Iolite software (Paton et al. 2011), and internal standardization was based on ^{57}Fe using the mean iron contents in the minerals as determined by electron microprobe. For the calibration of PGE and Au, the certified reference material Po727, a synthetic FeS doped with approximately 40 ppm of each PGE and Au, provided by the Memorial University of Newfoundland was employed. For the remaining elements, we used the certified reference material MASS-1, a ZnCuFeS pressed power pellet provided by the United States Geological Survey (USGS) and doped with 50–70 ppm Ag, As, Co, Bi, Sb, Se and Te (Wilson et al. 2002). Two in-house reference materials, JB-MSS5 and UQAC-MSS-1, were used to monitor the accuracy of the calibration. Analyses of the in-house reference materials agreed with the certified and working values (Table 1). ^{101}Ru was corrected for ^{61}Ni^{40}Ar interference using UQAC-MSS1: the correction is equivalent to 0.8 ppm in pentlandite and less than the lower limit of detection in pyrrhotite, pyrite and chalcopyrite. The amount of Cu interference on ^{103}Rh and ^{105}Pd from ^{63}Cu^{40}Ar and ^{65}Cu^{40}Ar, respectively, was determined by running a (CuFe)S$_2$ blank at the beginning and end of each session. In all phases except chalcopyrite, the Cu corrections on Rh and Pd are below the lower limit of detection. The interference of Cu arguide on ^{103}Rh in chalcopyrite exceeds 50 % of the Rh signal and thus Rh is not reported in chalcopyrite. Lower limit of detection for LA-ICP-MS analyses was calculated as three sigma background counts for the gas blank and each sulfide analyses. Tables with the individual analyses for pyrrhotite, pentlandite, chalcopyrite, and pyrite are provided in Tables 2, 3, 4, and 5, respectively.

Maps of the element distribution were made on sulfide aggregates composed of pyrrhotite, pentlandite, chalcopyrite, and pyrite using a beam size of 15 μm and a stage movement speed of 12 μm/s. A laser frequency of 15 Hz and a power of 4–6 J/cm^2 were used to map the aggregates in their entirety. The maps were then generated using the Iolite software package on the basis of the time-resolved composition of each element.

Pyrite textures

In all studied samples of the four mines, base metal sulfides occur as disseminations of polymineralic aggregates, up to several millimetres across, interstitial to the silicate framework (Fig. 3a). Generally, the igneous host rocks are orthopyroxenites composed of >80 wt% sub- to idiomorphic cumulus orthopyroxene with minor plagioclase, clinopyroxene, quartz, K-feldspar, and phlogopite as interstitial phases. Secondary phases are very minor (<5 wt%) and include actinolite, talc, chlorite, epidote, and carbonates. In the disseminated sulfides, pentlandite forms coarse grains or minor flame-shaped exsolution lamellae within pyrrhotite. Chalcopyrite typically occurs along the peripheries of sulfide aggregates and as isolated monomineralic grains.

Previous studies found that pyrite in the MSZ of the Great Dyke predominantly occurs associated with or within pyrrhotite (Oberthür 2011), as typically observed in other magmatic sulfide ore deposits worldwide such as Aguablanca (Piña et al. 2013) and Sudbury (Dare et al. 2011). In this study, we differentiate two textural types of pyrite: Py1 present in Ngezi and Hartley mines and Py2 from Unki and Mimosa mines.

Py1 forms fine symplectitic intergrowths with pentlandite and chalcopyrite occurring rarely within pyrrhotite (Fig. 3b–d). Locally, the Py1 crystals seem to have coalesced during their growth resulting in poikiloblastic aggregates that enclose chalcopyrite and pentlandite (Fig. 3b). These symplectitic textures between pyrite, pentlandite, and chalcopyrite resemble those described by Gervilla and Kojonen (2002) from the Keivitsansarvi Ni-Cu-PGE sulfide deposit in Finland, by Lorand and Alard (2011) in orogenic peridotites of the French Pyrenees, and by Naldrett et al. (2009) in the UG-2 reef of the Bushveld Complex, South Africa.

Py2 forms small individual euhedral or subhedral blocky crystals within pyrrhotite, pentlandite and, to a lesser extent, within chalcopyrite and silicates (Fig. 3e–f). In these samples, actinolite alteration occurs at the boundaries between silicates and sulfides. Silicate–sulfide contacts are less sharp than in the case of unaltered aggregates and sulfide grains, particularly chalcopyrite, occur along cleavage planes of actinolite (Fig. 3g). Epidote also occurs replacing plagioclase. In one sample from Unki (sample AS-5221), magnetite occurs in microfractures in pentlandite that also hosts heterogeneous pyrite crystals (Fig. 3h).

Table 1 Values for reference materials used in the calibration of LA-ICP-MS and analyses of in-house reference materials for monitoring the data quality

Isotope	34S (%)	57Fe (%)	59Co (ppm)	61Ni (%)	65Cu (%)	68Zn (ppm)	75As (ppm)	82Se (ppm)	101Ru (ppm)	103Rh (ppm)	105Pd (ppm)	107Ag (ppm)	111Cd (ppm)	121Sb (ppm)	125Te (ppm)	185Re (ppm)	189Os (ppm)	193Ir (ppm)	195Pt (ppm)	197Au (ppm)	209Bi (ppm)
Reference materials used for calibration of pyrrhotite, pentlandite, chalcopyrite, and pyrite																					
(material)	po-727	po-727	mass-1	jbmss5	mass-1	mass-1	mass-1	mass-1	po-727	po-727	po-727	mass-1	mass-1	mass-1	mass-1	jbmss5	po-727	po-727	po-727	po-727	mass-1
Working values	39	61.1	60	10.5	13.4	210000	65	51	36.3	41.4	43.1	50	60	60	15	20.7	46.9	47.8	35.4	45.8	60
S.D	0.4	0.2	10	0.01	0.05	5000	3	4	0.3	0.3	0.4	5	7	9		0.4	2.5	1.2	0.8	2.3	
Based on	Certif.	Certif.	Certif.	AR-AA	Certif.	Certif.	Certif.	Certif.	Certif.	Certif.	Certif.	Certif.	Certif.	Certif.	Certif.	ID-sol	Certif.	Certif.	Certif.	Certif.	Certif.
Values obtained for in-house reference materials																					
UQAC-MSS1, NiFeS2																					
Working values	38.00	30.30	n.d.	31.0	0.003	n.d.	1.90	5.30	1.75	0.94	1.26	0.25	0.27	0.08	0.19	0.09	1.90	1.37	1.66	1.21	<0.02
S.D.	0.50	1.30		0.7	0.001		0.21	0.35	0.03	0.01	0.05	0.08	0.06	0.03	0.06	0.00	0.01	0.01	0.01	0.24	
Based on	EMP	EMP		EMP	Nist610		Nist610	Nist610	ID-sol	po-727	ID-sol	Nist610	Nist610	Nist610	Nist610	ID-sol	ID-sol	ID-sol	ID-sol	Nist610	Nist610
This study average n=22	37.5	Int std	318	33.1	0.002	8.9	4.43	4.14	2.99	0.87	1.00	0.10	0.32	0.10	0.20	0.10	1.41	1.26	1.20	0.98	0.01
S.D.	1.3		42.0	1.24	0.001	3.0	2.57	0.68	0.34	0.06	0.14	0.04	0.29	0.06	0.20	0.01	0.11	0.11	0.18	0.20	0.00
Rel. Diff.	0.99			1.07	0.67		2.33	0.78	1.71	0.93	0.79	0.40	1.19	1.25	1.06	1.11	0.74	0.92	0.72	0.81	0.00
JBMSS5, FeS																					
Working values	40.57	57	5.03		0.021	13	79.0	61.1	21.70	64.80	59.70	53.0	0.20	61.30	40.57		42.60	40.65	35.80	35.90	76.10
S.D.	0.60	0.90	1.00		0.001	10	11.0	11.0		0.76	1.20	4.9	0.16	7.30	4.80		4.80	0.67	0.52	4.80	2.9
Based on	po727	po727	mass-1		ISS-4	mass-1	AR-ICP	mass-1	ID-sol	FA-ICP	FA-ICP	AR-ICP	mass-1	AR-ICP	mass-1		FA-ICP	FA-ICP	FA-ICP	AR-ICP	AR-ICP
This study average n=22	41.3	Int std	8.79		0.020	7.0	67.75	61.1	21.73	63.56	54.77	51.30	0.37	55.35	39.78		57.06	41.46	39.50	37.79	63.86
S.D.	1.0	1.4	1.4		0.011	3.9	9.47	6.5	1.45	2.79	1.89	8.19	0.31	3.79	18.22		5.42	3.59	1.35	2.47	5.30
Rel. Diff.	1.02		1.75		0.95	0.54	0.86	1.00	1.00	0.98	0.92	0.97	1.85	0.90	0.98		1.34	1.02	1.10	1.05	0.84

Po-727 is a certified synthetic FeS supplied by the Memorial University of Newfoundland. Mass-1 is a FeCuZnS pressed powder pellet supplied by USGS. Jbmss5 is a synthetic FeS in-house reference material supplied by J. Brenan from the University of Toronto. UQAC-MSS1 is a synthetic NiFeS2 supplied by A. Peregoedova. *Certif.* value on the certificate, *Nist610* laser ablation using Nist610 for calibration, *ID-sol* solution by isotopic dilution followed by ICP-MS, *EMP* electron microprobe, *AR-AA* aqua regia solution followed by atomic absorbition analysis, *AR-ICP* aqua regia solution followed by ICP-MS analysis, *FA-ICP* Ni-FA-co-percipitation followed by ICP-MS, *S.D.* standard deviation, *n.d.* not determined, *Int std* internal standard, *n* number of analyses, *Rel. Diff.* relative difference of this study/working value

Concentrations of PGE and other elements in BMS

Pyrrhotite, pentlandite, and chalcopyrite

The highest PGE contents were measured in pyrrhotite and pentlandite from the Hartley mine with pyrrhotite containing 1.1 to 3.0 ppm Ir and 1.6 to 3.7 ppm Ru and pentlandite containing up to 14.7 ppm Ru, 127.9 ppm Rh, 9.0 ppm Pt, and from 44.5 to 227.9 ppm Pd (Tables 2 and 3). In most cases, the laser ablation signal is quite stable (Fig. 4a) suggesting that PGE are in solid solution within sulfide grains. In a few cases, the ICP-MS signal shows well-developed narrow Os-Ir-Ru-(Pt) peaks (Fig. 4b) probably corresponding to microinclusions of discrete IPGE-bearing phases. In these cases, the microinclusions were excluded from the spectrum when determining the concentrations of the elements, so the PGE contents reported here are considered to be in solid solution within sulfides. These high PGE values in pyrrhotite and pentlandite from Hartley contrast with the low contents registered in pyrrhotite and pentlandite from Ngezi, Unki, and Mimosa mines. At these localities, pyrrhotite hosts less than 0.3 and 2 ppm Ir and Ru, respectively, and Rh, Os, and Pt are below their respective detection limits (<0.04 ppm Rh, <0.1 ppm Os, and <0.05 ppm Pt). Pentlandite contains up to 5.1 ppm Ru (typically <3 ppm), less than 1 ppm Rh, and Os and Ir are typically below the detection limit. Palladium in pentlandite from Ngezi, Unki, and Mimosa ranges from 4.7 to 271 ppm (generally <40 ppm). At Ngezi, pentlandite hosts appreciable though variable amounts of Pt (up to 6.2 ppm). The low PGE abundances in pentlandite observed in the present study in comparison to the Pd contents reported by Oberthür et al. (1997) (up to 2236 ppm Pd and 259 ppm Rh from the lower PGE subzone at Hartley, Unki, and Mimosa), Oberthür et al. (2003) (up to 2506 ppm Pd and 562 ppm Rh in pentlandite from the lower part of the PGE subzone at Hartley), and Locmelis et al. (2010) (up to 6500 ppm Pd in pentlandite at Hartley) are consistent with the provenance of samples from the Pt-peak of the MSZ, near to the transition between the PGE and BMS subzones (Fig. 2), since Pd contents in pentlandite oscillate between 500 and 1500 ppm Pd through most of the PGE subzone and drop to values around 40 ppm Pd when reaching the Pt peak. In all studied samples, chalcopyrite is poor in PGE with only trace amounts of Ru (0.2–0.4 ppm) and Pd (0.5–4.1 ppm) (Table 4). Regarding the other trace elements, Se contents are similar in sulfides from the four mines and range from 150.7 to 211.4 ppm Se in pyrrhotite, from 109.0 to 201.4 ppm Se in pentlandite, and from 93.6 to 133.7 ppm Se in chalcopyrite. Pentlandite hosts from 2485 to 9010 ppm Co and pyrrhotite contain between 2864 and 10690 ppm Ni and higher Co contents at Unki and Mimosa (73.2 to 260.4 ppm) compared to Hartley and Ngezi (32.8 to 90.0 ppm). In all sulfides, Au is below the detection limit (<0.08 ppm).

Pyrite

There are notable differences between the PGE abundances of Py1 from the Hartley and Ngezi mines and Py2 from the Mimosa and Unki mines (Table 5). Py1 is relatively rich in PGE: from 1.1 to 99.0 ppm Pt, 1.4 to 61.1 ppm Rh (Pt and Rh contents are typically >10 ppm), 1.7 to 47.1 ppm Ru, 0.1 to 7.8 ppm Os, and 1.2 to 20.2 ppm Ir. In contrast, PGE concentrations in Py2 are consistently low (<0.11 ppm Pt, <0.34 ppm Rh, <2.5 ppm Ru, <0.37 ppm Ir, and <0.40 ppm Os). Figure 4c shows a typical time resolved analyses (TRA) spectra of Py1 characterized by smooth, parallel patterns of Os, Ir, Ru, Rh, and Pt that suggests these PGE are really present in solid solution. Occasionally, the TRA spectra shows peaks of Os-Ir-Ru-(Rh) microinclusions (Fig. 4d) that were not considered during the data reduction. In the Hartley and Ngezi samples, the primitive mantle-normalized PGE patterns show that the PGE abundances in Py1 are generally higher than those in co-existing pyrrhotite and pentlandite with the exception of Rh in pentlandite from Hartley where Rh contents are notably higher (Fig. 5a–b). HAN-106 sample from Hartley is another exception where Py1 hosts similar amounts of Os, Ir, and Ru to pyrrhotite and pentlandite from a polymineralic grain (Fig. 5a). The PGE abundances in Py1 from Hartley analysed here are in agreement with previous data reported by Oberthür et al. (1997) from the Hartley mine using micro-pixe (40 ppm Ru, 10 ppm Rh, 9 ppm Pd, and 233 ppm Pt on average). In the Mimosa and Unki pyrites (Py2), the primitive mantle-normalized PGE patterns are very similar to those of pyrrhotite and pentlandite (Fig. 5c–d). Palladium in pyrite is commonly below 2 ppm in all studied samples except for some grains from Ngezi that contained up to 60.4 ppm Pd. Using all individual pyrite analyses from the four studied mines, Os, Ir, Ru, Rh, and Pt positively correlate with each other (Fig. 6a–c). In contrast, Pd poorly correlates with all other PGE. Gold, Te, Ag, Sb, and Bi contents are higher in Py2 from Mimosa and Unki compared to Py1 from Hartley and Ngezi (Fig. 5). Gold is positively correlated with Te and Bi (Fig. 6d), and Pt correlates positively with Au in Py1 from Hartley and Ngezi. Nickel contents in Py1 and Py2 are variable but they are typically below 2.5 wt% in both cases.

Compositional maps of two sulfide aggregates composed of pyrrhotite, pentlandite, chalcopyrite, and Py1 from the Hartley and Ngezi mines illustrate the trace element distribution among sulfide phases (Figs. 7 and 8). The maps indicate the relative concentration of the elements and are semi-quantitative. The Cu and Ni distribution mirrors the presence of chalcopyrite and pentlandite, respectively, whereas the Py1 is defined by elevated sulfur values. In both aggregates, Pt, Os, Ir, Ru, Co, Se, and Bi are preferentially concentrated in pyrite. Osmium, Ir, and Ru delineate almost perfectly the outlines of pyrite crystals. In Fig. 7, pyrite is also the main carrier of Rh and As, but in Fig. 8, Rh occurs preferentially in pentlandite and As is absent in all sulfide phases. Palladium concentrations are highest in pentlandite.

Table 2 Laser ablation ICP-MS results for individual pyrrhotite grains from different mines of the Great Dyke of Zimbabwe

Isotope	59Co (ppm)	61Ni (ppm)	65Cu (ppm)	66Zn (ppm)	75As (ppm)	187Re (ppm)	189Os (ppm)	193Ir (ppm)	101Ru (ppm)	103Rh (ppm)	195Pt (ppm)	105Pd (ppm)	197Au (ppm)	107Ag (ppm)	111Cd (ppm)	121Sb (ppm)	82Se (ppm)	209Bi (ppm)	125Te (ppm)
Hartley																			
HAN-106-1-2.D	46.8	5490	15.20	0.87	5.23	0.660	0.600	2.380	2.459	0.104	2.020	0.347	0.057	0.88	0.01	0.09	167.7	0.03	0.23
HAN-106-4-1.D	48.1	4560	2.05	1.12	3.48	0.031	0.626	2.227	3.674	0.165	0.091	0.428	0.082	0.20	0.00	0.06	211.4	0.00	0.03
HAN-106-5-2.D	32.8	3086	11.60	1.20	3.33	0.013	0.101	1.054	1.683	0.422	0.044	0.371	0.062	0.19	0.21	0.23	179.7	0.02	0.42
HAN-106-6-1.D	54.1	3790	3.90	0.79	3.50	0.224	0.836	3.010	1.679	0.074	0.068	0.389	0.058	0.14	0.33	0.06	193.6	0.01	0.19
HAN-106-8-1.D	44.3	3425	4.30	0.94	3.58	0.036	0.327	2.171	3.481	0.035	0.049	0.400	0.079	0.28	0.26	0.11	186.7	0.04	0.13
HAS-203-1-1.D	63.4	4420	2.83	0.92	2.15	0.025	0.308	1.440	3.635	0.038	0.056	0.371	0.307	0.23	0.20	0.08	150.7	0.02	0.13
HAS-203-2-2.D	58.9	3220	3.59	0.62	2.38	0.034	0.135	1.046	1.682	0.040	0.070	0.318	0.047	0.48	0.12	0.03	165.0	0.04	0.04
HAS-203-3-2.D	46.3	3460	3.89	0.39	2.20	0.085	0.672	1.795	3.661	0.042	0.062	0.413	0.070	0.18	0.13	0.01	157.9	0.00	0.49
HAS-203-4-1.D	89.0	5140	3.42	0.93	2.64	0.071	0.646	1.706	2.201	0.046	0.054	0.366	0.077	0.19	0.01	0.01	166.9	0.09	0.35
Ngezi																			
5863-4-4.D	55.6	6920	67.00	2.28	4.98	0.017	0.249	0.287	0.220	0.048	0.061	0.435	0.073	0.38	0.44	0.40	190.8	0.07	0.30
5860-1-3.D	90.0	7400	350.00	2.10	4.50	0.021	0.163	0.024	1.859	0.242	0.059	0.463	0.078	2.09	0.17	0.19	171.7	0.84	0.17
Mimosa																			
5535-1-1.D	174.2	8060	5.20	0.86	3.71	0.016	0.082	0.015	1.245	0.026	0.047	0.271	0.073	0.66	0.24	0.02	180.4	2.48	0.31
5535-1-2.D	170.0	4770	170.00	4.54	3.89	0.049	0.099	0.015	1.353	0.037	0.048	0.292	0.063	0.30	0.42	0.02	193.1	1.79	0.22
5535-2-1.D	162.2	10690	0.85	0.61	3.76	0.273	0.215	0.017	1.140	0.039	0.030	0.360	0.052	0.16	0.00	0.05	174.7	0.39	0.12
5535-5-2.D	177.0	5770	467.00	1.96	3.81	0.017	0.143	0.017	1.228	0.108	0.024	0.297	0.079	0.37	0.28	0.01	192.4	1.62	0.26
5535-6-2.D	125.3	5540	8.00	0.55	3.92	0.011	0.171	0.017	1.159	0.043	0.047	0.414	0.101	0.14	0.17	0.01	186.4	0.32	0.61
5535-7-2.D	260.4	9260	51.10	5.27	3.00	0.170	0.203	0.017	2.038	0.031	0.041	0.316	0.235	0.26	1.58	0.06	206.2	0.24	0.66
Unki																			
5221-1-3.D	77.0	3840	3.60	6.80	6.70	0.300	0.079	0.017	0.978	0.038	0.062	0.313	0.059	0.45	0.18	1.07	166.8	1.15	1.37
5221-2-3.D	87.1	3840	14.20	2.38	3.40	0.148	0.118	0.021	0.948	0.042	0.042	0.354	0.089	0.30	0.29	0.55	172.3	0.19	1.21
5221-3-2.D	97.0	7700	46.00	2.15	4.23	0.007	0.112	0.019	0.185	0.049	0.035	0.388	0.084	0.77	0.21	0.50	192.3	0.53	0.85
5221-4-1.D	73.2	5020	1.67	1.40	3.60	0.065	0.103	0.018	0.404	0.042	0.056	0.395	0.073	0.34	0.13	0.39	168.9	0.52	0.50
5221-6-2.D	130.4	6200	1.02	0.81	4.48	0.228	0.148	0.124	0.655	0.039	0.053	0.400	0.090	0.09	0.30	0.23	169.6	0.19	0.63
6041-1-2.D	107.8	3598	2.17	0.61	3.03	0.007	0.141	0.016	1.700	0.042	0.046	0.324	0.088	0.07	0.19	0.01	195.8	0.46	0.31
6041-2-2.D	122.1	5160	1.40	0.92	2.88	0.010	0.081	0.019	1.221	0.034	0.028	0.266	0.068	0.05	0.17	0.02	176.2	0.36	0.14
6041-5-1.D	149.1	9250	1.01	1.08	4.06	0.115	0.189	0.197	1.288	0.035	0.039	0.324	0.076	0.05	0.08	0.00	161.7	0.45	0.74
6041-6-2.D	131.0	9210	0.96	0.71	2.92	0.261	0.188	0.015	1.278	0.029	0.043	0.302	0.087	0.13	0.02	0.01	167.0	0.27	0.98
6041-8-3.D	156.1	6980	36.00	0.86	2.79	0.012	0.181	0.020	2.281	0.028	0.041	0.315	0.076	0.10	0.05	0.03	172.6	0.40	0.80
5222-2-1.D	87.2	2864	1.41	2.31	2.16	0.010	0.054	0.017	0.059	0.034	0.044	0.283	0.043	0.11	0.14	0.10	134.4	0.54	0.56
5222-3-1.D	125.6	5720	0.65	1.17	1.92	0.351	0.411	0.216	1.728	0.053	0.102	0.405	0.073	0.08	0.15	0.16	193.4	0.18	0.21
5222-4-2.D	170.0	5620	0.74	1.33	2.09	0.128	0.177	0.078	1.289	0.043	0.062	0.389	0.074	0.26	0.15	0.05	177.4	0.32	0.39
5222-8-1.D	135.5	5790	1.26	2.00	2.36	0.013	0.132	0.018	0.918	0.040	0.074	0.376	0.076	0.46	0.11	1.07	174.6	2.84	2.10

Values in italics correspond to limit of detection

Table 3 Laser ablation ICP-MS results for individual pentlandite grains from different mines of the Great Dyke of Zimbabwe

Isotope	59Co (ppm)	61Ni (ppm)	65Cu (ppm)	66Zn (ppm)	75As (ppm)	187Re (ppm)	189Os (ppm)	193Ir (ppm)	101Ru (ppm)	103Rh (ppm)	195Pt (ppm)	105Pd (ppm)	197Au (ppm)	107Ag (ppm)	111Cd (ppm)	121Sb (ppm)	82Se (ppm)	209Bi (ppm)	125Te (ppm)
Hartley																			
HAN-106-1-3.D	5390	324100	1.9	0.90	3.67	0.095	*0.102*	0.399	0.700	0.269	6.740	76.7	*0.066*	0.63	*0.01*	0.02	123.4	0.03	0.04
HAN-106-2-1.D	5100	311100	1.9	0.97	3.75	0.115	0.850	1.710	4.200	33.000	0.221	44.5	*0.056*	2.34	0.18	0.04	150.8	0.20	*0.01*
HAN-106-4-2.D	5340	323400	2.3	1.25	3.61	0.470	0.640	1.810	4.850	20.340	5.610	69.5	*0.066*	1.53	*0.01*	0.16	163.4	0.13	0.24
HAN-106-4-3.D	5720	299000	190.0	1.62	2.93	0.015	0.168	3.220	1.070	24.100	9.000	53.9	*0.045*	4.21	0.25	0.08	169.5	2.21	0.27
HAN-106-5-3.D	5880	312200	7.1	0.60	3.04	0.344	0.217	0.700	2.600	15.760	1.860	139.8	*0.057*	1.49	0.08	0.03	152.2	0.01	0.13
HAN-106-6-2.D	6350	320500	2.0	0.77	2.85	0.137	0.805	3.600	6.880	33.680	3.750	170.1	*0.048*	1.26	0.17	0.04	162.4	0.01	0.54
HAN-106-7-1.D	5900	315200	1.7	1.16	2.54	0.180	0.792	3.070	7.320	53.400	3.830	159.2	*0.057*	0.89	0.02	1.37	134.4	0.02	0.09
HAN-106-8-2.D	5870	314000	2.1	0.85	2.64	0.009	0.184	2.880	1.750	70.300	2.280	135.0	*0.066*	2.14	*0.01*	0.09	112.8	0.15	0.14
HAS-203-1-2.D	6980	319300	1.4	0.56	1.99	0.032	0.456	1.734	8.930	126.900	3.880	227.9	*0.055*	1.39	0.14	0.02	137.2	0.01	0.29
HAS-203-2-1.D	8010	309400	2.0	0.98	2.44	0.034	0.684	1.567	7.020	95.900	4.350	161.9	*0.052*	1.23	0.29	1.80	188.0	0.15	0.36
HAS-203-3-3.D	6730	299000	330.0	1.11	2.06	0.291	*0.073*	0.389	0.480	0.507	3.030	92.1	*0.061*	0.94	0.11	0.09	130.3	0.07	0.30
HAS-203-4-2.D	8670	309800	1.6	1.01	2.42	0.127	1.640	3.510	14.660	41.500	*0.039*	188.9	*0.053*	0.99	0.30	0.01	135.8	0.09	2.43
Ngezi																			
5863-1-2.D	2485	320200	3.7	1.20	5.03	0.034	*0.105*	*0.020*	*0.142*	0.330	6.190	176.5	*0.060*	2.38	0.26	0.18	174.3	0.30	2.03
5863-4-3.D	4440	343000	89.0	2.18	4.77	0.031	*0.108*	*0.022*	*0.138*	0.171	4.120	153.4	*0.062*	0.84	0.54	53.00	164.3	0.26	0.13
5860-1-1.D	5230	277000	11.5	35.00	5.21	0.011	*0.123*	*0.027*	*0.171*	1.230	*0.052*	146.0	*0.073*	1.99	2.40	3.60	145.0	7.80	0.69
5860-3-1.D	4340	344000	41.0	1.82	3.92	0.102	*0.112*	*0.025*	0.390	1.001	1.980	271.0	*0.078*	2.00	*0.01*	8.60	168.5	0.16	0.70
Mimosa																			
5535-2-2.D	5910	357100	1.1	0.78	3.36	0.063	*0.085*	*0.013*	2.090	0.447	*0.036*	11.3	*0.046*	0.23	0.15	0.05	158.0	0.13	11.96
5535-3-3.D	5860	351600	184.0	8.30	4.02	0.029	0.475	0.320	3.340	0.770	0.300	7.2	0.313	0.89	0.27	1.32	158.7	3.51	4.56
5535-5-4.D	5380	361000	780.0	4.20	3.59	0.127	0.356	*0.021*	2.290	0.884	*0.029*	6.9	0.317	0.62	0.13	0.12	201.4	1.24	3.25
5535-7-3.D	8140	358000	17.0	5.20	2.53	0.086	0.143	0.110	2.320	0.540	0.073	9.6	0.348	0.36	0.14	0.42	194.7	0.41	11.32
Unki																			
5221-1-2.D	6460	337300	1630.0	6.55	3.52	0.210	0.112	*0.018*	1.750	*0.031*	*0.029*	5.2	*0.051*	1.60	0.16	0.58	140.0	1.37	1.60
5221-6-3.D	8220	366600	44.0	2.09	3.99	0.015	*0.126*	*0.021*	1.320	0.108	*0.048*	4.7	*0.074*	0.24	*0.01*	0.57	131.1	0.52	4.11
6041-2-1.D	7480	342100	1.0	0.57	22.60	0.011	*0.054*	*0.016*	2.750	0.061	*0.029*	8.8	*0.066*	0.37	0.05	0.17	183.4	0.36	23.90
6041-5-2.D	5840	350400	3.2	1.41	4.64	0.099	0.162	*0.009*	5.090	*0.023*	*0.030*	6.0	*0.060*	1.48	0.12	0.21	144.6	0.19	9.64
6041-6-1.D	4910	262000	760.0	2.66	4.26	0.207	0.128	0.131	1.090	0.168	*0.033*	4.4	*0.039*	0.96	0.04	0.79	134.3	8.60	8.90
6041-7-3.D	5990	351000	45.0	1.53	3.88	0.007	*0.078*	*0.008*	1.170	*0.024*	*0.035*	5.7	*0.063*	0.68	0.10	0.23	144.0	2.25	5.45
6041-8-2.D	7280	353600	161.0	5.20	4.93	0.640	0.264	0.172	0.980	0.125	*0.023*	5.7	*0.052*	0.39	0.14	0.17	109.0	0.92	4.81
6041-9-2.D	6110	343000	0.9	1.12	5.51	0.006	*0.085*	*0.016*	2.530	*0.031*	*0.031*	6.4	*0.059*	1.44	0.06	0.05	147.3	0.01	15.20
5222-3-2.D	8100	344100	1.8	4.83	2.51	0.008	0.212	0.088	1.180	6.810	*0.043*	22.2	*0.048*	0.65	0.06	1.20	147.2	0.37	16.80
5222-5-1.D	7760	343500	2.0	6.80	4.30	0.046	0.150	0.053	1.210	3.380	*0.041*	21.8	0.102	0.64	0.07	1.35	187.9	0.42	49.20
5222-4-1.D	9010	329600	1.5	2.60	2.24	0.078	*0.084*	0.053	0.790	0.439	*0.063*	37.6	*0.075*	0.40	0.10	2.10	118.6	0.10	5.71
5222-8-2.D	6530	334500	1.2	2.50	1.61	0.016	*0.089*	*0.020*	0.900	*0.033*	*0.060*	4.6	*0.054*	0.37	0.06	0.07	125.1	0.55	2.41

Values in italics correspond to limit of detection

Table 4 Laser ablation ICP-MS results for individual chalcopyrite grains from different mines of the Great Dyke of Zimbabwe

| Isotope	59Co (ppm)	61Ni (ppm)	65Cu (ppm)	66Zn (ppm)	75As (ppm)	187Re (ppm)	189Os (ppm)	193Ir (ppm)	101Ru (ppm)	103Rh (ppm)	195Pt (ppm)	106Pd (ppm)	197Au (ppm)	107Ag (ppm)	111Cd (ppm)	121Sb (ppm)	82Se (ppm)	209Bi (ppm)	125Te (ppm)
Hartley																			
HAN-106-1-4.D	54.0	3640	319500	553	3.70	*0.002*	*0.065*	*0.013*	0.324	n.a.	*0.040*	1.337	*0.052*	26.7	15.0	0.04	93.6	0.01	0.07
HAN-106-8-3.D	14.2	1340	325300	800	3.01	*0.006*	*0.053*	*0.016*	0.315	n.a.	*0.045*	1.042	*0.049*	22.4	16.9	0.02	109.2	0.01	0.21
HAS-203-1-3.D	3.6	1130	328700	596	2.60	*0.003*	*0.067*	*0.014*	0.298	n.a.	*0.037*	0.956	*0.051*	12.4	24.4	0.09	111.1	0.02	0.01
HAS-203-4-3.D	91.0	5100	337400	514	2.66	*0.008*	*0.083*	0.320	0.890	n.a.	*0.045*	3.008	*0.067*	9.8	22.5	0.04	110.8	0.23	0.18
HAS-203-6-1.D	1.3	867	340600	700	2.30	*0.000*	*0.072*	*0.020*	0.270	n.a.	*0.038*	1.334	*0.045*	11.7	27.8	0.07	116.6	0.02	0.43
Ngezi																			
5863-2-3.D	0.2	911	330900	684	5.90	*0.001*	*0.092*	*0.018*	0.237	n.a.	*0.034*	0.714	*0.063*	0.5	18.2	0.02	107.6	0.01	0.26
5860-1-2.D	4.2	1127	332500	567	5.32	*0.002*	*0.099*	*0.017*	0.329	n.a.	*0.038*	0.472	*0.055*	0.4	8.1	7.20	98.3	0.22	0.16
Mimosa																			
5535-4-1.D	0.5	941	329300	1530	3.75	*0.008*	*0.077*	*0.010*	0.331	n.a.	*0.032*	1.103	0.470	9.2	24.0	0.01	116.0	1.11	0.58
5535-6-1.D	0.6	894	324000	505	3.64	*0.014*	*0.060*	*0.011*	0.354	n.a.	*0.030*	0.587	1.710	15.1	10.9	0.06	133.7	0.58	0.46
5535-7-1.D	1.1	915	332100	535	2.98	*0.022*	*0.061*	*0.015*	0.387	n.a.	*0.035*	0.618	0.294	4.4	12.1	0.02	152.0	0.76	0.54
Unki																			
5221-2-2.D	33.9	950	334600	515	3.44	*0.003*	*0.067*	*0.017*	0.403	n.a.	*0.025*	0.816	*0.039*	1.4	18.6	0.62	112.9	0.89	1.15
5221-4-2.D	0.3	857	332300	534	3.37	*0.001*	*0.086*	*0.013*	0.387	n.a.	*0.036*	1.094	*0.051*	0.9	23.7	0.20	111.8	0.59	3.20
5221-6-1.D	0.2	864	338600	631	3.08	*0.003*	*0.082*	*0.022*	0.368	n.a.	*0.040*	1.380	*0.064*	1.1	28.4	0.17	116.1	1.20	1.73
6041-1-1.D	2.2	889	319000	589	3.16	*0.001*	*0.076*	*0.009*	0.392	n.a.	*0.028*	0.581	*0.061*	1.5	13.5	0.04	133.3	1.83	0.85
6041-1-3.D	3.8	955	321100	540	3.06	*0.001*	*0.065*	*0.012*	0.351	n.a.	*0.031*	0.509	*0.053*	1.4	11.7	0.03	117.6	0.60	0.77
6041-8-1.D	0.4	836	337900	1020	2.45	*0.006*	*0.052*	*0.014*	0.332	n.a.	*0.039*	0.958	*0.051*	0.9	21.4	0.05	118.5	0.38	0.50
5222-1-1.D	0.2	866	332600	1640	2.39	*0.002*	*0.081*	*0.017*	0.272	n.a.	*0.044*	1.734	*0.051*	5.8	23.6	0.01	116.6	0.78	2.62
5222-2-2.D	2.0	1140	324800	1870	1.87	*0.001*	*0.054*	*0.017*	0.321	n.a.	0.402	5.999	*0.043*	1.5	24.2	0.02	123.9	4.89	16.30
5222-4-3.D	0.3	856	331500	1640	2.52	*0.001*	*0.085*	*0.019*	0.304	n.a.	0.580	4.034	*0.050*	0.8	20.1	0.02	125.3	3.44	9.24
5222-8-3.D	61.0	5140	327800	1341	1.74	*0.002*	*0.082*	*0.015*	0.286	n.a.	*0.044*	1.074	*0.061*	1.1	25.4	0.44	132.0	1.24	1.58

Values in italics correspond to limit of detection. *N.a.* not analyzed

Table 5 Laser ablation ICP-MS results for individual pyrite grains (Py1 and Py2) from different mines of the Great Dyke of Zimbabwe

Isotope	59Co (ppm)	61Ni (ppm)	65Cu (ppm)	66Zn (ppm)	75As (ppm)	187Re (ppm)	189Os (ppm)	193Ir (ppm)	101Ru (ppm)	103Rh (ppm)	195Pt (ppm)	105Pd (ppm)	197Au (ppm)	107Ag (ppm)	111Cd (ppm)	121Sb (ppm)	82Se (ppm)	209Bi (ppm)	125Te (ppm)
Hartley - Py1																			
HAN-106-2-3.D	26500	4510	2560	45.0	11.1	0.061	0.100	1.220	1.675	2.311	3.93	0.531	0.047	0.93	1.11	0.10	272.0	1.95	0.32
HAN-106-5-1.D	15860	990	40200	80.0	27.0	0.269	0.219	2.190	3.304	13.253	11.32	<0.116	0.097	4.80	1.62	0.20	261.6	9.41	0.51
HAN-106-9-2.D	16720	6300	9600	76.0	25.3	0.127	0.540	2.670	3.775	1.435	12.20	2.411	0.090	2.34	0.96	0.27	226.5	5.40	0.51
HAS-203-3-1.D	11850	2330	6800	18.4	22.2	0.157	6.320	16.300	27.687	2.406	33.10	<0.196	0.196	3.60	0.67	0.35	213.4	16.52	0.60
HAS-203-5-1.D	6350	1910	540	23.5	11.9	0.215	7.800	19.300	47.089	9.150	25.90	<0.169	0.144	2.55	0.46	0.27	223.0	24.50	0.76
HAS-203-5-2.D	8240	3700	6400	30.2	9.7	0.106	7.070	20.200	41.279	11.004	19.40	<0.183	0.158	2.91	1.05	0.20	234.0	20.70	0.54
Ngezi - Py1																			
5863-1-1.D	4270	4760	23200	38.8	9.5	0.074	2.760	10.440	16.423	19.038	63.00	3.650	0.194	3.81	1.11	0.05	195.1	24.30	1.45
5863-1-3.D	1770	6100	3250	11.3	11.8	0.061	2.310	17.500	25.266	39.197	89.00	7.305	0.113	1.33	0.39	0.11	204.0	11.74	1.53
5863-1-4.D	2060	18500	7800	22.0	8.3	0.051	1.770	6.440	12.566	16.673	99.00	10.171	0.139	3.52	0.85	0.59	229.8	20.50	4.65
5863-2-1.D	3750	3860	41900	153.0	11.6	0.075	2.230	8.800	17.078	61.095	12.15	<0.174	5.100	8.10	3.50	0.09	196.0	26.80	1.34
5863-4-1.D	4100	8050	5600	25.4	13.8	0.073	1.610	5.600	9.555	13.398	2.90	<0.172	0.062	2.05	0.33	0.30	277.0	10.40	0.44
5863-4-2.D	4380	4920	7000	26.0	70.0	0.075	1.440	4.460	5.162	35.648	14.10	0.588	0.145	2.01	0.77	0.51	178.4	30.80	1.30
5863-5-1.D	402	2030	2750	13.6	7.8	0.044	1.870	6.290	9.189	2.394	1.14	0.526	<0.036	0.93	0.44	1.51	237.0	3.51	0.19
5863-5-2.D	840	1670	13700	17.3	5.8	0.040	1.580	5.000	12.29	6.123	6.65	<0.150	0.153	4.00	0.98	2.00	225.0	11.90	0.81
5863-6-1.D	3370	5210	750	24.4	29.0	0.050	2.250	6.880	12.27	13.830	2.53	0.305	0.096	0.69	0.37	0.13	292.7	9.90	1.12
5860-2-1.D	850	3170	36100	75.0	7.7	0.067	2.050	8.370	11.782	19.835	10.71	<0.163	0.184	4.27	1.43	0.15	204.1	22.43	1.17
5860-3-2.D	10310	51300	870	23.2	6.1	0.083	3.260	16.210	29.813	54.819	13.60	55.641	0.074	2.13	0.36	0.45	187.6	35.30	1.00
5860-PY.D	6550	151000	1070	6.8	6.2	0.050	2.290	1.790	10.354	31.000	24.90	60.404	0.062	1.59	0.24	1.76	193.0	28.00	0.79
Mimosa - Py2																			
5535-3-1.D	7120	5540	23060	16.6	3.9	0.280	0.194	0.021	1.083	0.125	0.063	0.145	0.780	16.11	0.62	0.25	217.9	210.70	14.66
5535-3-2.D	5710	5270	5210	23.2	3.7	0.049	0.148	<0.005	1.158	0.025	0.070	0.114	0.565	12.65	0.98	1.58	247.6	253.00	2.54
5535-5-1.D	8570	7120	34200	34.1	6.9	0.033	0.133	<0.005	1.113	0.163	0.042	<0.127	0.513	11.70	1.06	0.21	267.3	112.00	5.70
5535-5-3.D	7920	12100	9800	8.2	2.8	0.013	0.113	<0.004	0.832	0.047	0.058	0.365	0.293	4.98	0.25	0.09	284.0	27.00	5.17
Unki - Py2																			
5221-1-1.D	11460	3200	12860	51.1	18.8	0.225	0.138	<0.006	1.057	0.053	<0.014	0.154	0.254	16.10	1.90	1.94	218.3	143.50	17.10
5221-2-1.D	9590	25700	17050	172.0	22.4	0.100	0.105	<0.005	0.738	0.091	<0.011	0.976	0.444	130.00	8.69	2.91	221.3	89.00	17.60
5221-3-1.D	6320	35700	41000	61.3	25.6	0.020	0.069	<0.006	0.292	0.089	<0.010	1.149	0.420	48.90	4.76	3.82	268.9	159.50	87.90
6041-3-1.D	12400	22900	380	15.6	74.0	0.039	0.237	0.202	1.522	0.115	0.011	0.880	0.305	1.96	0.22	0.30	129.8	51.50	21.00
6041-4-1.D	10010	3020	21800	34.8	45.2	0.290	0.146	0.208	0.965	0.278	0.117	0.666	0.581	13.01	1.21	2.06	246.0	60.00	56.20
6041-4-2.D	3220	10780	11000	23.2	37.8	0.139	0.128	0.185	1.230	0.325	0.106	0.695	0.289	7.43	0.74	1.92	177.5	40.80	37.30
6041-7-1.D	3920	7310	11400	17.8	14.6	0.061	0.180	0.157	1.399	0.058	<0.018	<0.152	0.381	16.60	0.63	0.45	226.0	187.00	28.10
5222-6-1.D	2190	11970	3040	26.0	9.1	0.074	0.217	0.159	1.513	0.300	<0.018	0.303	0.063	1.75	0.25	0.50	281.8	14.20	2.84
5222-6-2.D	10760	108000	41200	176.0	20.3	0.370	0.399	0.370	2.495	0.340	<0.027	1.282	0.960	11.88	3.90	3.05	252.5	301.00	23.30
5222-7-1.D	5280	32700	21600	143.0	55.0	0.009	0.198	0.044	1.177	<0.022	<0.025	<0.166	0.436	19.10	1.16	0.69	269.8	99.00	20.80

Less than sign indicates below the detection limit

Fig. 3 Representative photomicrographs in reflected light showing the sulfide assemblage with different pyrite textures of the Main Sulfide Zone in the Great Dyke of Zimbabwe. **a** Disseminated sulfides located interstitially to orthopyroxene (Opx) composed by pyrrhotite (Po), pentlandite (Pn), and chalcopyrite (Cpy), sample 6041b, Unki mine. **b–c** Irregular pyrite (Py1) grains intergrowth in chalcopyrite and minor pentlandite, sample 5863b, Ngezi mine. **d** Symplectitic-type textures between pyrite (Py1) and pentlandite and chalcopyrite, sample 5863b, Ngezi mine. **e** Porous pyrite (Py2) grain situated within pentlandite, sample 5535, Mimosa mine. **f** Blocky euhedral to subhedral pyrite (Py2) grains within pentlandite, sample 6041b, Unki mine. **g** Chalcopyrite along cleavage planes of actinolite, sample 5535, Mimosa mine. **h** Pyrite (Py2) and magnetite (Mgt) anhedral crystals within pentlandite, sample AS-5221, Unki mine
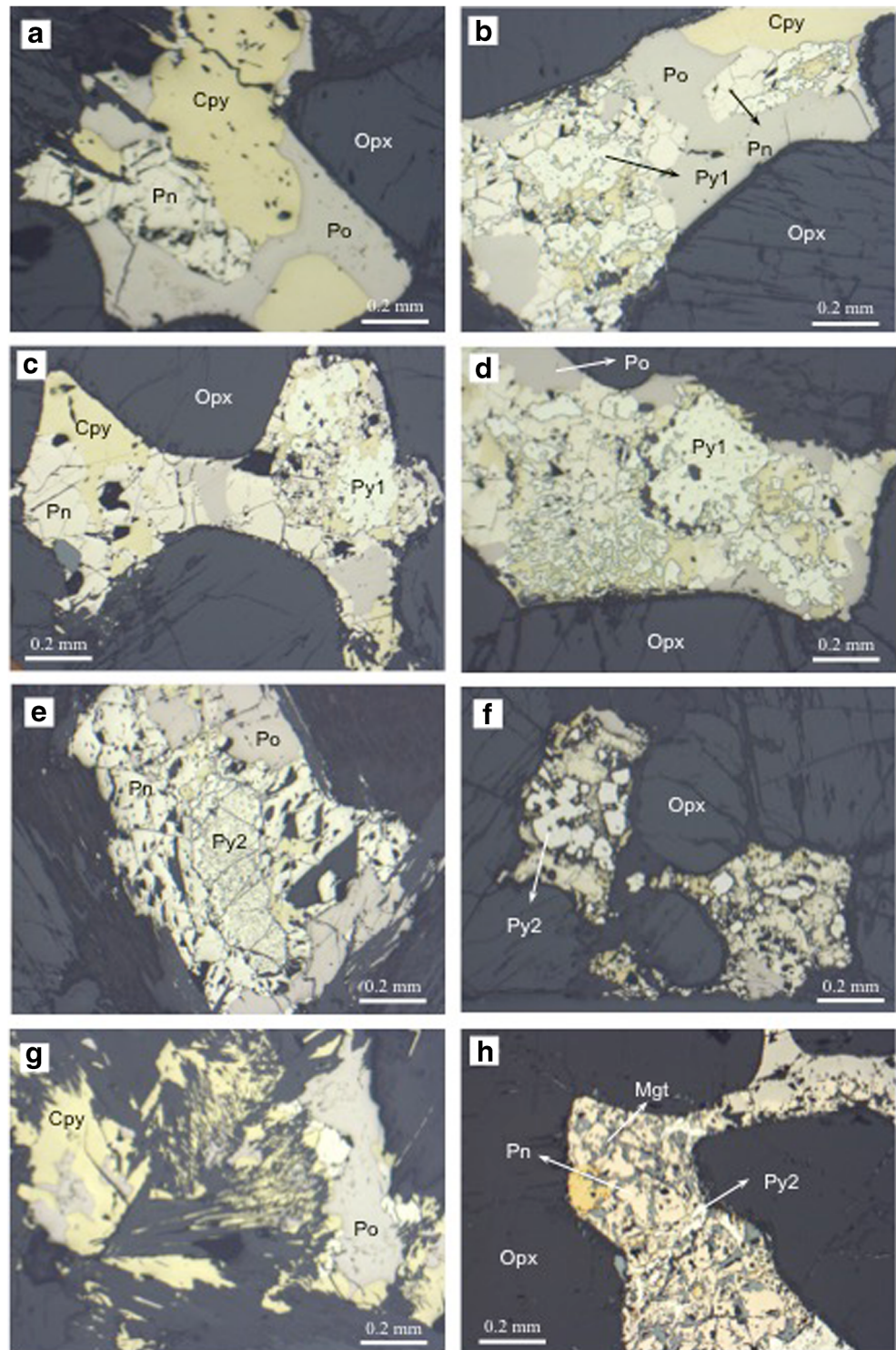
Discussion

Mechanisms of pyrite formation

The formation of pyrite in Ni-Cu-(PGE) magmatic sulfide deposits is commonly attributed to the activity of late magmatic or hydrothermal fluids that trigger the replacement of pre-existing sulfides (mostly pyrrhotite) by pyrite due to increase of sulfur activity (i.e., increasing fS_2) or removal of Fe (Oberthür 2002, 2011; Djon and Barnes 2012; Piña et al. 2013; Smith et al. 2014; Holwell et al. 2014; Duran et al. 2015). For example, hydration of igneous silicates (pyroxene and plagioclase) leads to the formation of secondary hydrous silicates such as chlorite, actinolite, and epidote decreasing the H_2O content of the fluids. This leads
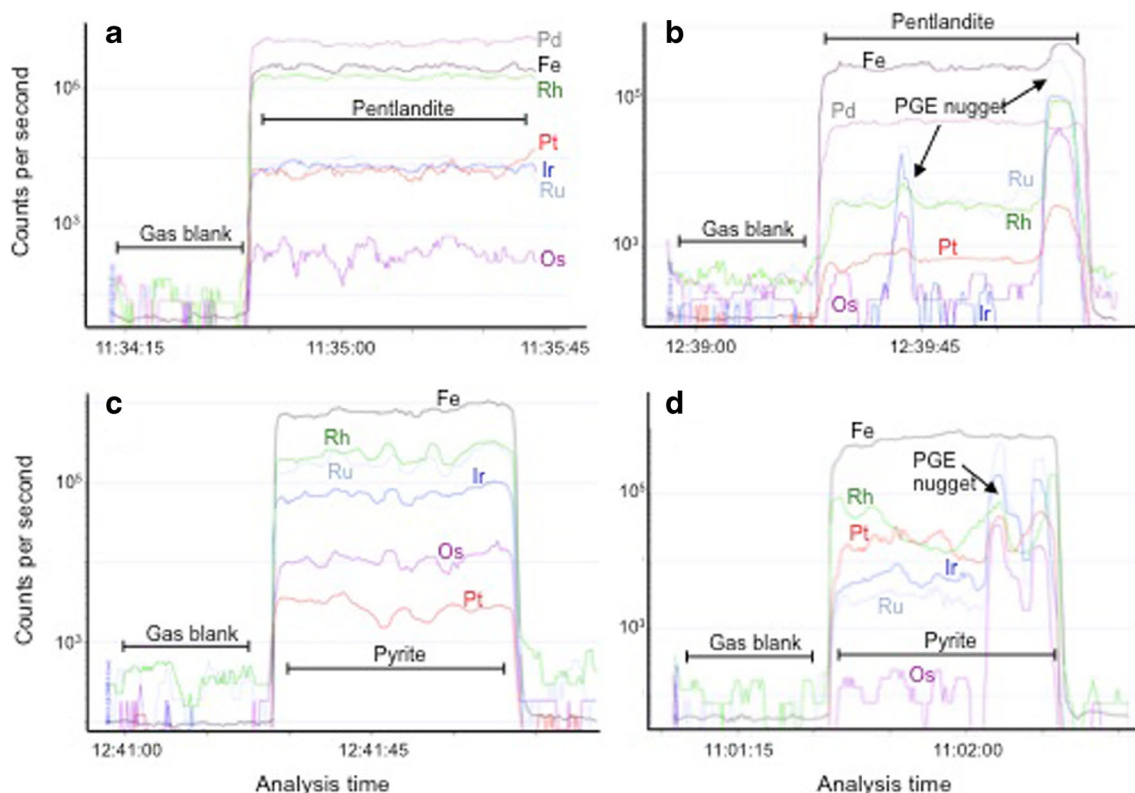
Fig. 4 Selected time resolved analysis (TRA) spectra for LA-ICP-MS lines ablated across **a** pentlandite (analyses no. HAN-106-6.2, Hartley mine), **b** pentlandite (analyses no. 5860–3.1, Ngezi mine), **c** pyrite (Py1, analyses no. 5860–3.2, Ngezi mine), and **d** pyrite (Py1, analyses no. HAN-106-2.3, Hartley mine). Note that TRA spectra labeled (**a**) and (**c**) do not show any PGE-bearing microinclusion, whereas spectra (**b**) and (**d**) exhibit PGE-bearing nuggets. In these cases, the microinclusions were excluded from the spectrum when determining the concentrations of the elements

to an increase in S and fS$_2$ of the fluids driving the stabilization of pyrite over pyrrhotite (Kanitpanyacharoen and Boudreau 2013). Pyrite can also form by loss of Fe from pyrrhotite to surrounding chlorite, actinolite, or chromite. Previous studies in the Great Dyke of Zimbabwe noted that pyrite predominately replaces pyrrhotite, and its abundance increases upward through the BMS subzone of the MSZ sequence (Oberthür 2002; Li et al. 2008). This observation led Oberthür (2002) to suggest a general trend of upward increasing fS$_2$ within the MSZ. According to Li et al. (2008), the increase in fS$_2$ that triggered the replacement of pyrrhotite by pyrite in the MSZ took place as a consequence of the release of S from the underlying zone upward due to extensive actinolite alteration. Based on sulfur isotope values of pyrite, which range from 0.4 to 1 ‰ δ^{34}S, Li et al. (2008) suggested that the fluids involved in the formation of pyrite were of a reduced nature (H$_2$S-bearing). In our Unki and Mimosa samples, Py2 occurs as blocky grains inside pentlandite, pyrrhotite (Fig. 3e–f), and to a lesser extent, among silicate grains, and the primary silicate assemblage is relatively altered as shown by the presence of actinolite and epidote at the contacts between orthopyroxene or plagioclase and sulfides, respectively. This observation suggests that Py2 in these samples is likely secondary and formed during episodes of late magmatic and/or hydrothermal alteration as described above.

In the Hartley and Ngezi samples, Py1 is intimately associated with pentlandite and chalcopyrite, in some cases in form of symplectitic intergrowths, and is texturally not related to pyrrhotite (Fig. 3b–d), although pyrrhotite is present in the aggregates. Furthermore, these pyrite-bearing sulfide aggregates do not show any evidence of alteration by hydrothermal fluids such as the presence of hydrous silicates as epidote or actinolite between silicates and sulfides. These features are regarded relevant for the origin of pyrite and raise uncertainty as to whether these Py1 are the result of replacement as has been interpreted at Mimosa and Unki or form part of the original assemblage developed during crystallization and cooling of a high temperature sulfide melt. If hydrothermal fluids had played some role in the formation of pyrite, then the alteration mechanism must explain the replacement of pentlandite and chalcopyrite (but not pyrrhotite) by pyrite. Similar pyrite, pentlandite, and chalcopyrite intergrowth textures have been early described in other deposits by Gervilla and Kojonen (2002), Lorand and Alard (2011), and Naldrett et al. (2009). In all these cases, pyrite occurs associated with pentlandite and/or chalcopyrite locally forming fine symplectitic intergrowths. At Keivitsansarvi, Gervilla and Kojonen (2002) propose that with the drop of temperature below 230 °C Ni-rich MSS decomposed forming pyrite and pentlandite. Lorand and Alard (2011) suggest that the formation
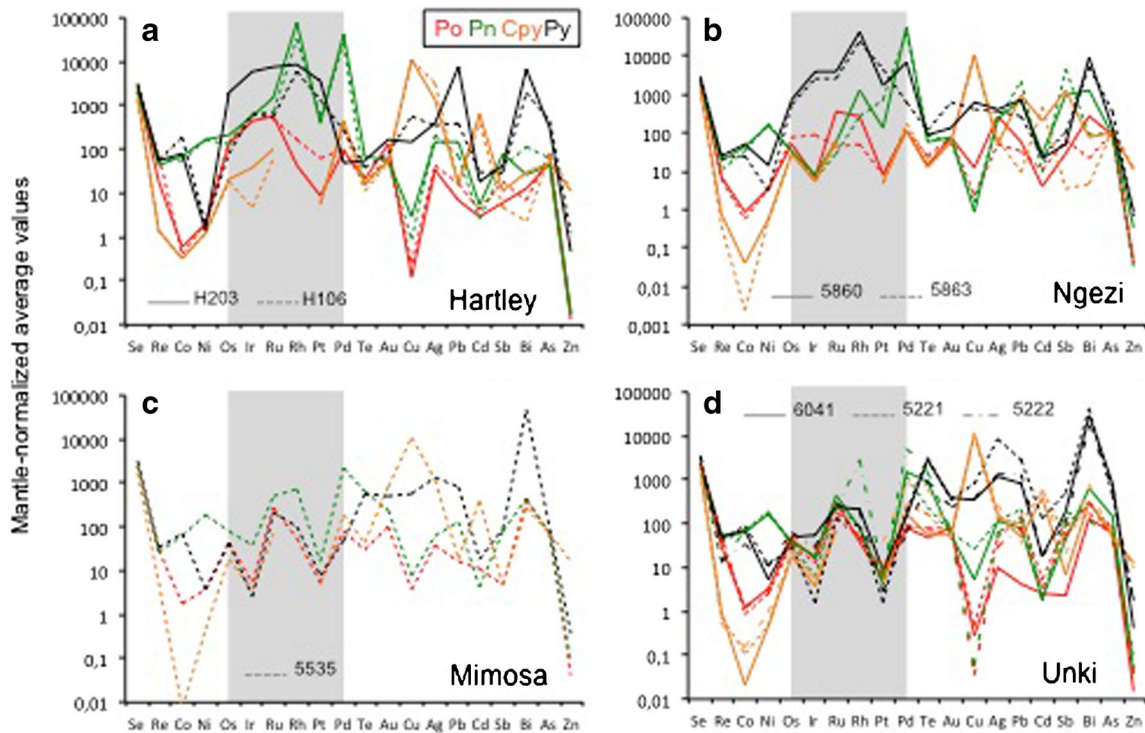
Fig. 5 Primitive mantle-normalized trace element profiles for average contents in pyrrhotite (Po, *red*), pentlandite (Pn, *green*), chalcopyrite (Cpy, *orange*), and pyrite (Py, *black*) in different samples for Hartley (**a**), Ngezi (**b**), Mimosa (**c**), and Unki (**d**) mines. Normalizing values are those of McDonough and Sun (1995). Elements were ordered in decreasing order of compatibility into MSS. The *grey shade* highlights the PGE
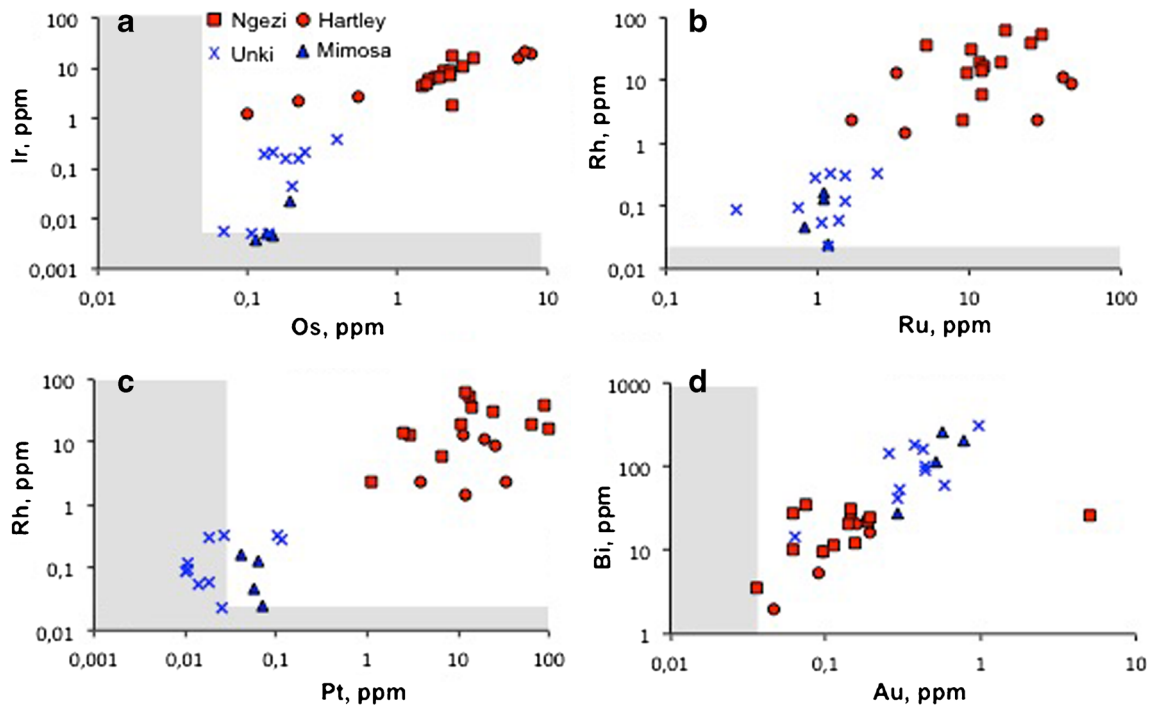

Fig. 6 Binary plots showing positive correlations between individual abundances in pyrite grains: **a** Os vs. Ir, **b** Ru vs. Rh, **c** Rh vs. Pt, and **d** Au vs. Bi. When the obtained value was below the detection limit, this value was represented. *Grey shades* mean values below the detection limit. Note that Py1 from Hartley and Ngezi has distinctly higher contents of Os, Ir, Ru, Rh, and Pt than Py2 from Unki and Mimosa. Notably, Py2 from Unki and Mimosa is richer in Bi and Au than Py1 from Hartley and Ngezi
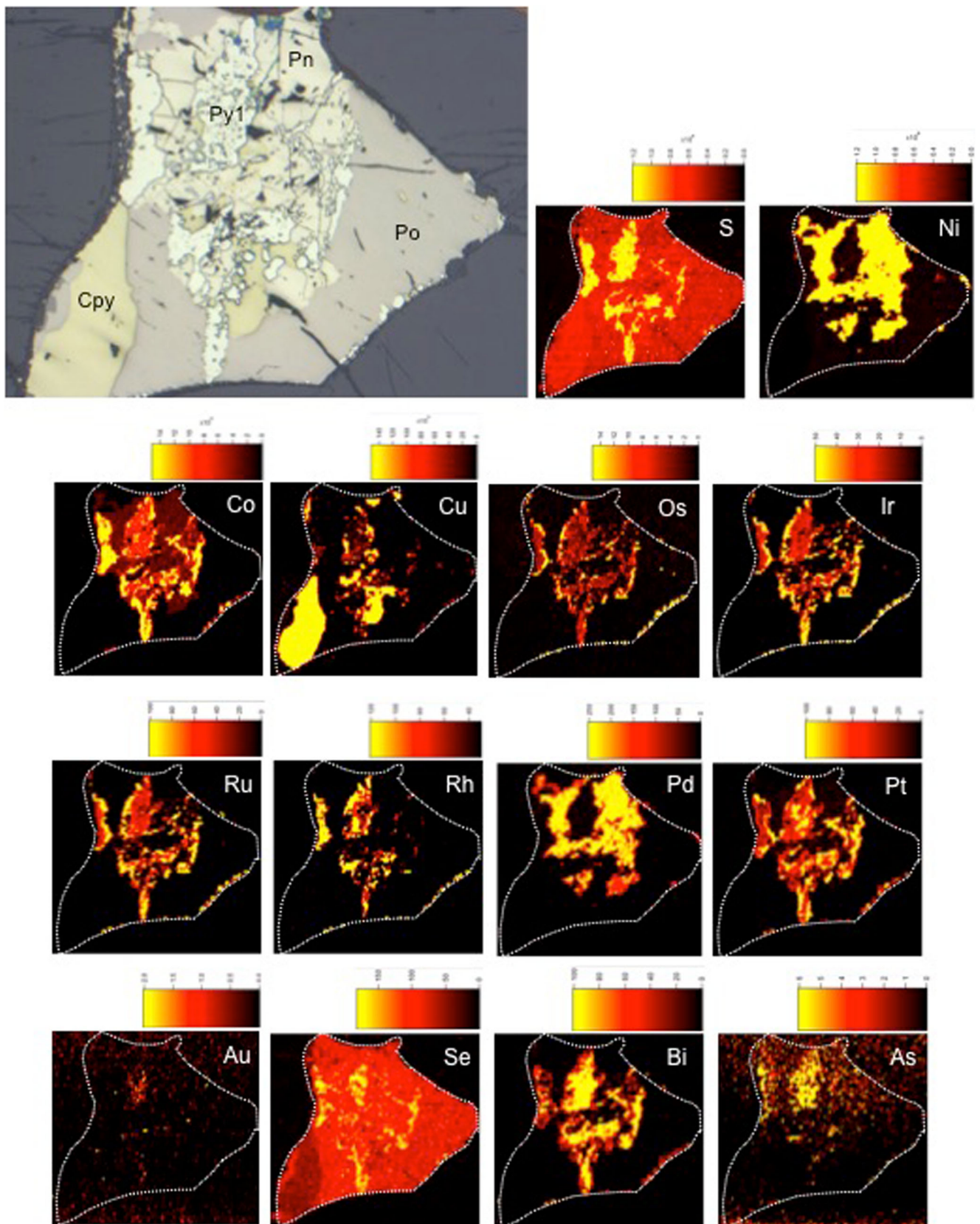
Fig. 7 Element distribution maps between coexisting pyrrhotite, pentlandite, chalcopyrite, and Py1 (sample 5863, Ngezi mine). Mapping was carried out by 15 μm-sized line scans ablating the whole aggregate. The maps show semi-quantitative values. Cobalt, Os, Ir, Ru, Rh, Pt, Se, Bi, and As are preferentially concentrated in Py1 whereas Pd preferentially concentrates in pentlandite

of pyrite intergrowths with pentlandite and chalcopyrite in orogenic peridotites from the French Pyrenees was due to subsolidus sulfurization processes that increased the fS_2 of the system as a consequence of addition of external S. Lorand and Alard (2011) propose that pentlandite was first transformed into Ni-rich MSS at temperatures above 300 °C which then exsolved to pentlandite + pyrite symplectites during cooling below 300 °C. According to Lorand and Alard (2011), symplectite intergrowths between chalcopyrite, pyrite, and pentlandite probably formed from Cu-rich MSS. In the case of the UG-2 reef, Naldrett et al. (2009) suggest that on cooling, removal of Fe from sulfides to chromite generated a significant rise in fS_2 of the system. The sulfur-enriched sulfide liquid crystallized first at 900 °C as a Ni-rich MSS in equilibrium with a Cu-rich liquid. On further cooling, the Ni-rich MSS gave rise to the pentlandite and pyrite assemblage whereas the liquid solidified very rapidly crystallizing in the form of ISS-pyrite symplectites.

It is suggested here that the pyrite-pentlandite intergrowths observed in the Hartley and Ngezi samples probably formed during low-temperature equilibration of a Ni-rich MSS. The pentlandite composition is closely related to the sulfide minerals with which the pentlandite is associated. Experimental studies in the system Fe-Ni-S at 230 °C (Misra and Fleet 1973) and the tentative <135 °C Fe-Ni-S phase diagram indicate that pentlandite coexisting with pyrite is relatively rich in Ni (Naldrett et al. 2009). Indeed, pentlandite in the pentlandite-pyrite assemblages from the Great Dyke is relatively rich in Ni with [Fe:(Fe + Ni)] ratios (in wt. %) ranging from 0.46 to 0.49. These ratios are further similar to those observed in pentlandite equilibrated with pyrite and pyrrhotite in the Marbridge deposit, Quebec (Graterol and Naldrett 1971), where it was empirically demonstrated the existence of a stable tie-line between pentlandite and pyrite in the Fe-Ni-S system at low temperatures. In any event, the pyrite-pentlandite symplectitic intergrowth points to an equilibration temperature below the maximum stability of pentlandite with pyrite, which is reported to be below 280 °C (Misra and Fleet 1973) and 213 ± 12 °C (Craig 1973).

Pyrite as host of PGE

According to the PGE concentrations measured in the present study, two types of pyrite are differentiated in the Great Dyke of Zimbabwe: (i) PGE-rich Py1 present in the Hartley and Ngezi samples and (ii) PGE-poor Py2 present in the Unki and Mimosa samples. All samples were taken approximately from the Pt-peak of the MSZ, so this difference cannot be attributed to the general vertical PGE geochemical zonation present in the MSZ profiles (e.g., Prendergast and Wilson 1989; Oberthür 2002, 2011). The primitive mantle-normalized PGE patterns shown in Fig. 5 seem to indicate a close relationship between the PGE concentrations of Py1 and Py2 and the concentrations of coexisting pyrrhotite and pentlandite. The Ngezi samples represent an exception. Despite

the low PGE contents in pyrrhotite and pentlandite (akin to Unki and Mimosa), pyrite is enriched in PGE with values even exceeding those of Hartley. As argued above, Py2 in the Unki and Mimosa samples is interpreted as having formed by partial replacement of pre-existing sulfides (mainly, pyrrhotite and pentlandite) due to the activity of late magmatic or hydrothermal fluids. During this process, pyrite likely inherited the low PGE contents of the replaced pyrrhotite and pentlandite as suggested for other Ni-Cu-PGE sulfide deposits (e.g., Dare et al. 2011; Djon and Barnes 2012; Piña et al. 2013; Smith et al. 2014).

According to partition coefficients between MSS and sulfide melt (Mungall et al. 2005) and empirical observations in several Ni-Cu and PGE ore deposits (e.g., Barnes and Ripley 2015), the IPGE (Os, Ir, and Ru) and Rh are expected to be present in solid solution within the products of MSS crystallization, namely, pyrrhotite and pentlandite. The lower concentrations of the IPGE in pyrrhotite and pentlandite of the Unki and Mimosa samples in comparison with pyrrhotite and pentlandite in the Hartley samples may indicate that in Unki and Mimosa sulfides formed from particularly PGE-depleted sulfide liquids. The role of the fractionation of sulfide liquid in the PGE distribution within the MSZ was noted by Oberthür (2002) who indicated that the low content of PGE inside sulfides of the BMS subzone of the MSZ in comparison with the sulfides of the PGE subzone (particularly, the drop of Pd in pentlandite from values of 500–1500 ppm through most of the PGE subzone to values below 40 ppm in the BMS subzone) is a consequence of the progressive depletion in PGE of the sulfide melt undergoing fractionation up-sequence. However, this interpretation must be taken with caution because the availability in the system of semimetals such as Bi, Te, Sb, or As exerts a notable influence on the redistribution and final mineralogical siting of the PGE (Helmy et al. 2007, 2013). Arsenic, Sb, Bi, and Te are poorly soluble in MSS and tend to concentrate in residual melts that coexist with the high temperature sulfides (Helmy et al. 2010; Liu and Brenan 2015). These semimetals are potent complexing agents for Pt and Pd so, when present, the As, Bi, and Te-rich melts scavenge PGE originally contained in the sulfide melt and avoid they enter the lattices of high-temperature sulfides. Finally, the decrease of temperature will result in the crystallization of PGE arsenides, tellurides, and bismuthotellurides often along grain-boundary triple junctions of base metal sulfides (Helmy et al. 2007; Holwell and McDonald 2007). As a consequence, the PGE content in sulfides will depend on the combination of different factors including the fractionation of the sulfide melt, the ability of each sulfide to incorporate PGE in their lattice and, importantly, the presence or not of PGE-ligand semimetals.

The results obtained from the Hartley and Ngezi samples highlight a feature previously documented in other Ni-Cu-PGE sulfide deposits that include pyrite in their sulfide
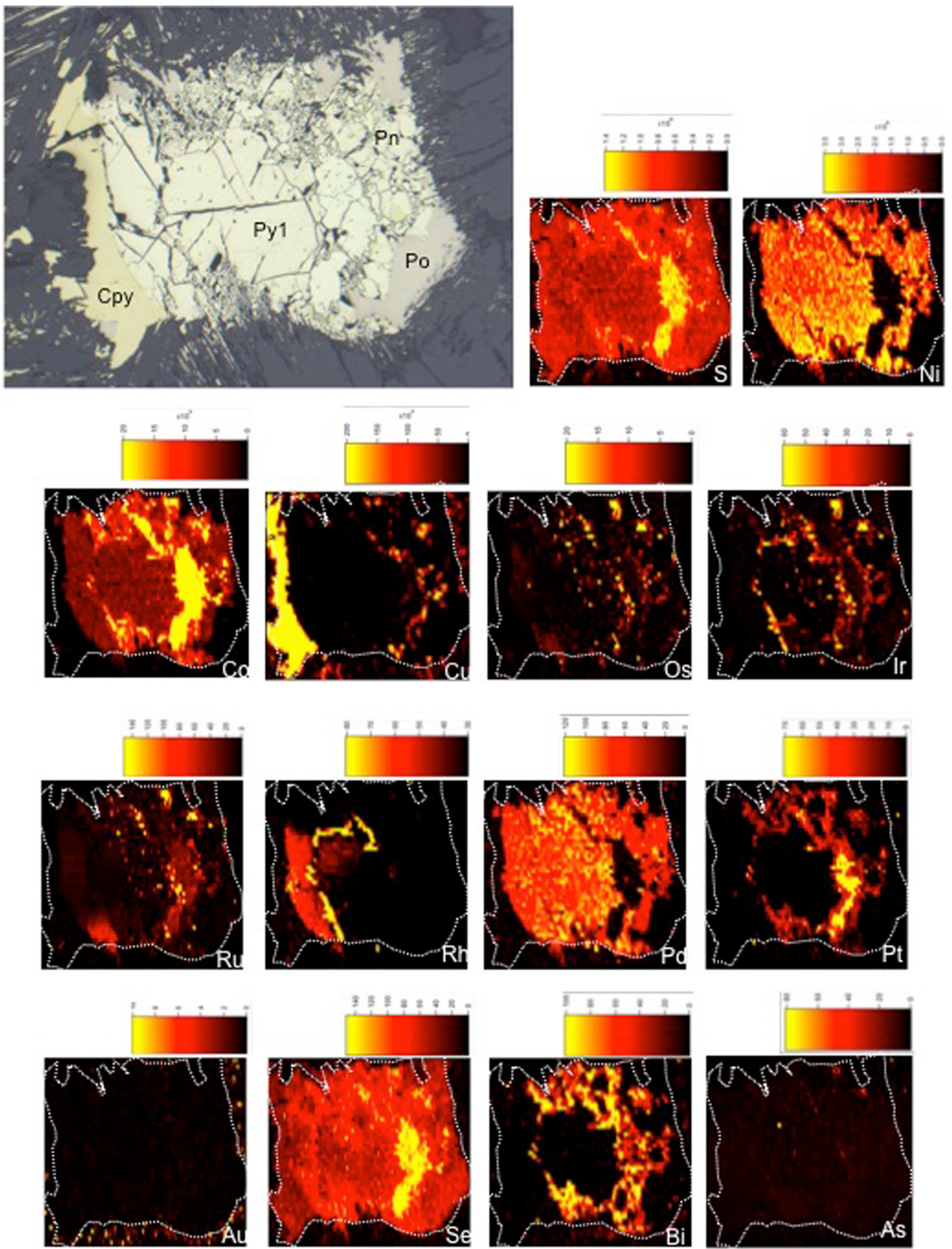
◀ **Fig. 8** Element distribution maps between coexisting pyrrhotite, pentlandite, chalcopyrite, and Py1 (sample HAN-106, Hartley mine). Mapping was carried out by 15 μm-sized line scans ablating the whole aggregate. The maps show semi-quantitative values. Cobalt, Os, Ir, Ru, Pt, Se, and Bi are preferentially concentrated in Py1. Palladium and Rh preferentially concentrate in pentlandite

assemblage: among all sulfides, pyrite is the most important host of Pt. At Aguablanca, individual zoned grains of pyrite are the only base metal sulfides to host this metal with contents up to 9 ppm Pt (Piña et al. 2013). Compared to co-existing pyrrhotite and pentlandite, accessory pyrite from the McCreedy East deposit in Sudbury is enriched in Pt with values ~0.1 ppm (Dare et al. 2011). At Lac des Iles, Ontario (Canada), Pt in all base metal sulfides, except pyrite, is below 0.1 ppm, but reaches values as high as 11 ppm in pyrite (Djon and Barnes 2012; Duran et al. 2015). The interpretation attributed to the presence of Pt in pyrite is quite analogous in all these cases. Because pyrite typically replaces pyrrhotite and pyrrhotite does not contain any Pt, it is interpreted that the hydrothermal fluids responsible of the replacement of pyrrhotite by pyrite may have dissolved some Pt-bearing PGM (e.g.,

moncheite and sperrylite) making Pt available for its incorporation into pyrite. In the Hartley and Ngezi samples, Py1 has elevated Pt contents (commonly > 10 ppm) compared to most other deposits. Platinum in these Py1 must have a different origin because this pyrite has been interpreted as primary, formed during low-temperature equilibration of sulfides, and in addition pentlandite in these samples, whose formation is not related to hydrothermal fluids, also hosts appreciable though variable amounts of Pt (up to 9 ppm, Table 3).

Nevertheless, despite the high Pt contents of the Py1, most of the Pt in the ores is not located in pyrite. For example, bulk concentrations of Pt in the studied samples HAN-106 and HAS-203 are 9496 and 9593 ppb, respectively. In these samples, visually-estimated modal abundances of pyrite do not exceed 2 modal % of the total minerals. Using an average content of Pt in pyrite of 9.2 ppm for the sample HAN-106 and 26.1 ppm for the sample HAS-203 (Table 5), the maximum contents of the total Pt budget accounted for pyrite would be 1.9 and 5.4 %, respectively. These numbers are consistent with previous studies indicating that Pt dominantly occurs in the form of discrete PGM (e.g., Oberthür et al. 2003). Indeed, there is a clear predominance of Pt-
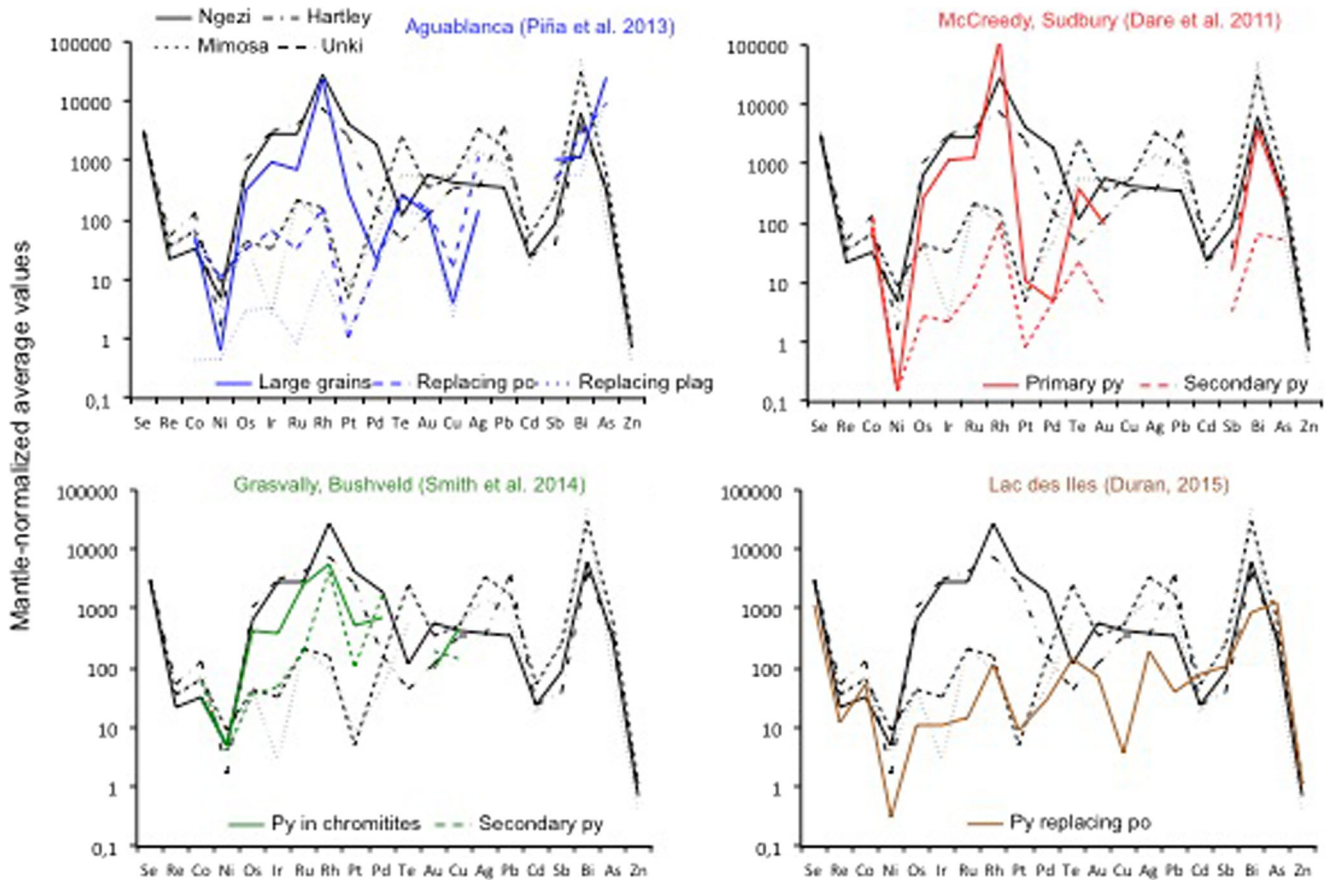

Fig. 9 Primitive mantle-normalized trace element profiles of average contents in pyrite from Hartley, Ngezi, Mimosa, and Unki and those for different textural types of pyrite from Aguablanca (**a**), McCreedy deposit (**b**), Grasvally (**c**), and Lac des Iles (**d**). Normalizing values of McDonough and Sun (1995). Data source for deposits: Aguablanca, Piña et al. (2013); McCreedy, Dare et al. (2011); Grasvally, Smith et al. (2014); and Lac des Iles, Duran et al. (2015). Elements were ordered in decreasing order of compatibility into MSS

dominated PGM (generally Pt bismuthotellurides, cooperite, and sperrylite) on Pd-dominated PGM in the MSZ of the Great Dyke (Barnes et al. 2008; Oberthür 2011) and, in fact, some discrete Pt-bearing PGM (typically moncheite) were identified during this study. Similarly, Dare et al. (2011) showed that the role of pyrite as carrier of Pt in the McCreedy East deposit is negligible (<0.5 %) and Djon and Barnes (2012) calculated that the most Pt-rich pyrites only account for about 5 % of total Pt in the Lac des Iles deposit. Therefore, we observe that the proportion of total Pt accounted by pyrite is probably relatively low because (1) pyrite is an accessory phase present in modal abundances typically below 10 % total sulfides; (2) although the amount of Pt is significant relative to pyrrhotite, pentlandite and chalcopyrite, the absolute contents are generally in the range of a few ppm only; and (3) various Pt-bearing PGM are generally present that account for the bulk of the whole rock Pt in these deposits.

Rhodium also occurs at high concentrations in pyrite of some Ni-Cu-PGE ore deposits (Djon and Barnes 2012; Dare et al. 2011; Piña et al. 2013; Smith et al. 2014; Duran et al. 2015). In contrast to Pt, Rh is not exclusively present in pyrite but also occurs in pentlandite. In fact, pentlandite is considered to be a major carrier of Rh in some Ni-Cu-PGE ore deposits (Barnes et al. 2008; Holwell and McDonald 2010; Junge et al. 2014, 2015). Several studies indicate that pyrite has a relevant role as carrier of Rh. For example, Dare et al. (2011) determined that in samples with accessory (<2 modal %) pyrite from the McCreedy East deposit, pyrite carries ~60 % of total Rh. Djon and Barnes (2012) noted that more than 60 % of the Rh budget resides in pyrite from disseminated sulfides from the Lac des Iles deposit. In the northern Bushveld (Grasvally), Smith et al. (2014) reported high Rh in pyrite (>54 ppm) probably accounting for a high proportion of the total. In the Great Dyke, the generally higher contents of Rh in pentlandite compared to pyrite and the predominance of pentlandite over pyrite suggest that pentlandite probably contains higher amounts of total Rh than pyrite. Hollingworthite (RhAsS) is the only Rh-bearing PGM identified in the Great Dyke and occurs in low proportions (<2 %) in the North chamber but is common of the South chamber where elevated proportions of PGE arsenides and sulfarsenides like sperrylite, hollingworthite, platarsite, and irarsite are present (Oberthür 2002, 2011). The Rh concentrations of pentlandite and Py1 in the North chamber are considerably higher (up to 127 ppm in pentlandite and 61 ppm in pyrite) than those in the South chamber (typically below 1 ppm in pentlandite and 0.4 ppm in pyrite), so it is probable that the proportion of total Rh residing in BMS are notably higher in the North chamber compared to the South chamber.

The mantle-normalized trace element profiles of pyrite from the Great Dyke and other Ni-Cu-PGE deposits (Fig. 9)

show that Co is notably enriched in pyrite compared to Ni and most pyrites exhibit pronounced positive anomalies of Rh. It is important to note that pyrite from the McCreedy deposit, interpreted as having formed by exsolution from MSS, is significantly enriched in IPGE and Rh compared to secondary pyrite formed by alteration of the MSS cumulates by late magmatic/hydrothermal fluids. This compositional difference in PGE abundances between primary and secondary pyrite resembles that observed in the Great Dyke samples. On the other hand, pyrite from Lac des Iles, Aguablanca and Grasvally, interpreted as alteration product of pre-existing sulfides (mostly pyrrhotite), in general, has PGE and other trace element contents similar to Py2 from Unki and Mimosa. These results suggest that primary Py1, formed during equilibration upon cooling of sulfide minerals, potentially hosts more PGE than secondary Py2, formed by alteration of pre-existing sulfides.

Conclusions

1. On the basis of textural features, PGE concentrations, and mode of formation, two types of pyrite (Py1 and Py2) can be differentiated in the MSZ from the Great Dyke of Zimbabwe.
2. Py1 contains high Os, Ir, Ru, Rh, and Pt concentrations (Pt and Rh > 10 ppm; 1.7 to 47.1 ppm Ru, 0.1 to 7.8 ppm Os, and 1.2 to 20.2 ppm Ir) and occurs forming cluster of small individual grains intimately intergrowth with pentlandite and chalcopyrite. This type of pyrite is interpreted as having formed by low temperature (<300 °C) decomposition of residual Ni-rich MSS. Py1 was found in our samples from the Hartley and Ngezi mines.
3. Py2 has low PGE concentrations (<0.11 ppm Pt, <0.34 ppm Rh, <2.5 ppm Ru, <0.37 ppm Ir, and <0.40 ppm Os), occurs as individual blocky grains within mainly pyrrhotite and pentlandite and is interpreted as having formed by replacement of pyrrhotite and pentlandite due to the activity of late magmatic/hydrothermal fluids. Py2 was identified in our samples from the Unki and Mimosa mines
4. Although the laser ablation ICP-MS analyses reveal that individual grains of pyrite can host relatively high contents of PGE, particularly up to 61 ppm Rh and 99 ppm Pt, even higher than coexisting pyrrhotite, pentlandite, and chalcopyrite in a same sulfide aggregate, the amount of total Rh and Pt that reside within pyrite is likely low (<5 %) and the bulk of the Pt budget (>95 %) resides in discrete PGM grains.

References

Ballhaus C, Sylvester P (2000) Noble metal enrichment processes in the Merensky Reef, Bushveld Complex. J Petrol 4:545–561

Barnes S-J, Lightfoot PC (2005) Formation of magmatic nickel sulfide deposits and processes affecting their copper and platinum group element contents. Econ Geol 100:179–213

Barnes S-J, Ripley EM (2015) Highly siderophile and strongly chalcophile elements in magmatic ore deposit. Reviews in Mineralogy and Geochemistry 81, in press

Barnes S-J, Cox RA, Zientek ML (2006) Platinum-group element, gold, silver and base metal distribution in compositionally zoned sulfide droplets from the Medvezky Creek Mine, Noril'sk, Russia. Contrib Mineral Petrol 157:187–200

Barnes S-J, Prichard HM, Cox RA, Fisher PC, Godel B (2008) The location of the chalcophile and siderophile elements in platinum-group element ore deposits (a textural, microbeam and whole rock geochemical study): Implications for the formation of the deposits. Chem Geol 248:295–317

Boudreau AE, Meurer WP (1999) Chromatographic separation of the platinum-group elements, gold, base metals and sulfur during degassing of a compacting and solidifying igenous cristal pile. Contrib Mineral Petrol 134:174–185

Craig JR (1973) Pentlandite-pyrrhotite and other low-temperature relations in the Fe-Ni-S systems. Am J Sci 273:496–510

Dare SAS, Barnes S-J, Prichard HM, Fisher PC (2011) Chalcophile and platinum-group element (PGE) concentrations in the sulfide minerals from the McCreedy East deposit, Sudbury, Canada, and the origin of PGE in pyrite. Miner Deposita 46:381–407

Djon MLN, Barnes S-J (2012) Changes in sulfides and platinum-group minerals with the degree of alteration in the Roby, Twilight, and High Grade Zones of the Lac des Iles Complex, Ontario, Canada. Miner Deposita 47:875–896

Duran CJ, Barnes S-J, Corkery JT (2015) Chalcophile and platinum-group element distribution in pyrites from the sulfide-rich pods of the Lac des Iles Pd deposits, Western Ontario, Canada: implications for post-cumulus re-equilibration of the ore and the use of pyrite composition exploration. J Geochem Explor 158:223–242

Gervilla F, Kojonen K (2002) The platinum-group minerals in the upper section of the Keivitsansarvi Ni-Cu-PGE deposit, northern Finland. Can Mineral 40:377–394

Godel B, Barnes S-J (2008) Platinum-group elements in sulfide minerals and the whole rocks of the J-M Reef (Stillwater Complex): implications for the formation of the reef. Chem Geol 248:272–294

Graterol M, Naldrett AJ (1971) Mineralogy of the Marbridge No. 3 & No. 4 Nickel-Iron Sulfide Deposits. Econ Geol 66:886–900

Helmy HM, Ballhaus C, Berndt J, Bockrath C, Wohlgemuth-Ueewasser C (2007) Formation of Pt, Pd and Ni tellurides: experiments in sulphide-telluride systems. Contrib Mineral Petrol 153:577–591

Helmy HM, Ballhaus C, Wohlgemuth-Ueewasser C, Fonseca ROC, Laurenz V (2010) Partitioning of Se, As, Sb, Te and Bi between monosulfide solid solution and sulfide melt-application to magmatic sulfide deposits. Geochim Cosmochim Acta 74:6174–6179

Helmy HM, Ballhaus C, Fonseca ROC, Nagel TJ (2013) Fractionation of platinum, palladium, nickel and copper in sulfide-arsenide systems at magmatic temperature. Contrib Mineral Petrol 166:1725–1737

Holwell DA, McDonald I (2007) Distribution of platinum-group elements in the Platreef at Overysel, northern Bushveld Complex: a combined PGM and LA-ICP-MS study. Contrib Mineral Petrol 154:171–190

Holwell DA, McDonald I (2010) A review of the behaviour of platinum group elements within natural magmatic sulfide ore systems. Platin Met Rev 54:26–36

Holwell DA, Keays RR, Firth EA, Findlay J (2014) Geochemistry and mineralogy of platinum-group element mineralization in the River Valley intrusion, Ontario, Canada: a model for early stage S saturation and multi-stage emplacement and the implications for 'contact-type' Ni-Cu-PGE mineralization. Econ Geol 109:689–712

Junge M, Oberthür T, Melcher F (2014) Cryptic variation of chromite chemistry, platinum-group element and platinum-group minerals distribution in the UG-2 chromitites: an example from the Karee Mine, western Bushveld Complex, South Africa. Econ Geol 109: 795–810

Junge M, Wirth R, Oberthür T, Melcher F, Schreiber A (2015) Mineralogical siting of platinum-group elements in pentlandite from the Bushveld Complex, South Africa. Miner Deposita 50:41–54

Kanitpanyacharoen W, Boudreau AE (2013) Sulfide-associated mineral assemblages in the Bushveld Complex, South Africa: platinum-group element enrichment by vapor refining by chloride-carbonate fluids. Miner Deposita 48:193–210

Kullerud G, Yund RA, Moh G (1969) Phase relations in the Fe-Ni-S, Cu-Fe-S and Cu-Ni-S systems. Econ Geol Monograph 4:323–343

Li C, Ripley EM, Oberthür T, Miller JD, Joslin GD (2008) Textural, mineralogical and stable isotope studies of hydrothermal alteration in the Main sulfide zone of the Great Dyke, Zimbabwe and the Precious Metals zone of the Sonju Lake intrusion, Minnesota, USA. Miner Deposita 43:97–110

Liu Y, Brenan J (2015) Partitioning of platinum-group elements (PGE) and chalcogens (Se, Te, As, Sb, Bi) between monosulfide-solid solution (MSS), intermediate solid solution (ISS) and sulfide liquid at controlled fO_2–fS_2 conditions. Geochim Cosmochim Acta 159: 139–161

Locmelis M, Melcher F, Oberthür T (2010) Platinum-group element distribution in the oxidized Main Sulfide Zone, Great Dyke, Zimbabwe. Miner Deposita 45:93–109

Lorand J-P, Alard O (2011) Pyrite tracks assimilation of crustal sulfur in Pyrenean peridotites. Mineral Petrol 101:115–128

McDonough WF, Sun SS (1995) The composition of the Earth. Chem Geol 120:223–253

Misra KC, Fleet ME (1973) The chemical composition of synthetic and natural pentlandite assemblages. Econ Geol 68:518–539

Mungall JE, Andrews DRA, Cabri LJ, Sylvester PJ, Tubrett M (2005) Partitioning of Cu, Ni, Au, and platinum-group elements between monosulfide solid solution and sulfide melt under oxygen and sulfur fugacities. Geochim Cosmochim Acta 69:4349–4360

Naldrett AJ (2004) Magmatic sulfide deposits: geology, geochemistry and exploration. Springer, Berlin, 727 pp

Naldrett AJ (2011) Fundamentals of magmatic sulfide deposits. In: Li C, Ripley EM (eds) Magmatic Ni–Cu and PGE deposits: Geology, Geochemistry, and Genesis. Society of Economic Geology. Rev Econ Geol 17:1–50

Naldrett AJ, Craig JR, Kullerud G (1967) The central portion of the Fe-Ni-S system and its bearing on pentlandite exsolution in iron-nickel sulfide ores. Econ Geol 62:826–847

Naldrett AJ, Kinnair J, Wilson A, Yudovskaya M, McQuade S, Chunnett G, Stanley C (2009) Chromite composition and PGE content of Bushveld chromitites: Part 1—the Lower and Middle Groups. Appl Earth Sci Trans Inst Min Metall B 118:131–161

Oberthür T (2002) Platinum-group element mineralization of the Great Dyke, Zimbabwe. CIM Spec 54:483–506

Oberthür T (2011) Platinum-group element mineralization of the Main Sulfide Zone, Great Dyke, Zimbabwe. In: Li C, Ripley EM (eds)

Magmatic Ni–Cu and PGE deposits: Geology, Geochemistry, and Genesis. Society of Economic Geology. Rev Econ Geol 17:329–349

Oberthür T, Cabri LJ, Weiser TW, McMahon G, Müller P (1997) Pt, Pd and other trace elements in sulfides of the main sulfide zone, Great Dyke, Zimbabwe: a reconnaissance study. Can Mineral 35:597–609

Oberthür T, Davis DW, Blenkinsop TG, Höhndorf A (2002) Precise U-Pb mineral ages, Rb-Sr and Sm-Nd systematics for the Great Dyke, Zimbabwe—constraints on late Archean events in the Zimbabwe craton and Limpopo belt. Precambrian Res 113:293–305

Oberthür T, Weiser TW, Gast L, Kojonen K (2003) Geochemistry and mineralogy of platinum-group elements at Hartley Platinum Mine, Zimbabwe. Miner Deposita 38:327–343

Paton C, Hellstrom J, Paul B, Woodhead J, Hergt J (2011) Iolite: freeware for the visualization and processing of mass spectrometric data. J Anal At Spectrom 26:2508–2518

Piña R, Gervilla F, Barnes S-J, Ortega L, Lunar R (2013) Platinum-group elements-bearing pyrite from the Aguablanca Ni-Cu sulfide deposit (SW Spain): a LA-ICP-MS study. Eur J Mineral 25:241–252

Prendergast MD (1987) The chromite ore field of the Great Dyke, Zimbabwe. In: Stowe CW (ed) Evolution of chromite ore fields. Van Nostrand, New York, pp 89–108

Prendergast MD (1998) The Great Dyke – mineral resources and mining development. In: Guidebook to the Great Dyke of Zimbabwe. 8th International Platinum Symposium, Johannesburg, South Africa. pp 10–15

Prendergast MD, Wilson AH (1989) The Great Dyke of Zimbabwe. II: Mineralization and mineral deposits. In: Prendergast MD, Jones MJ (eds) Magmatic sulfides – the Zimbabwe volume, Institution of Mining and Metallurgy, pp 21–42

Smith JW, Holwell DA, McDonald I (2011) The mineralogy and petrology of platinum-group element-bearing sulphide mineralization within the Grasvally Norite-Pyroxenite-Anorthosite (GNPA) member, south of Mokopane, northern Bushveld Complex, South Africa. Appl Earth Sci (Trans Inst Min Metall B) 120:B158–B174

Smith JW, Holwell DA, McDonald I (2014) Precious and base metal geochemistry and mineralogy of the Grasvally Norite-Pyroxenite-Anorthosite (GNPA) member, northern Bushveld Complex, South Africa: implications for a multistage emplacement. Miner Deposita 49:667–692

Vukmanovic Z, Reddy SM, Godel B, Barnes SJ, Fiorentini ML, Barnes S-J, Kilburn MR (2014) Relationship between microstructures and grain-scale trace element distribution in komatiite-hosted magmatic sulfide ores. Lithos 184–187:42–61

Wilson AH (1982) The geology of the Great Dyke, Zimbabwe: the ultramafic rocks. J Petrol 23:240–292

Wilson AH (1998) The Great Dyke – geological summary. In: Guidebook to the Great Dyke of Zimbabwe. 8th International Platinum Symposium, Johannesburg, South Africa. pp 1–10

Wilson AH (2001) Compositional and lithological controls on the PGE-bearing sulfide zones in the Selukbe subchamber, Great Dyke: a combined equilibrium-Rayleigh fractionation model. J Petrol 42:1845–1867

Wilson AH, Prendergast MD (1989) The Great Dyke of Zimbabwe – I. Tectonic setting, stratigraphy, petrology, structure, emplacement and crystallization. In: Prendergast MD, Jones MJ (eds) Magmatic sulfides – the Zimbabwe volume, Institution of Mining and Metallurgy, pp 1–20

Wilson AH, Tredoux M (1990) Lateral and vertical distribution of the platinum-group elements, and petrogenetic controls on the sulfide mineralization, in the P1 Pyroxenite layer of the Darwendale subchamber of the Great Dyke, Zimbabwe. Econ Geol 85:556–584

Wilson AH, Prendergast MD (2001) Platinum-group element mineralization in the Great Dyke, Zimbabwe, and its relationship to magma evolution and magma chamber structure. S Afr J Geol 104:319–342

Wilson SA, Ridley WI, Koenig AE (2002) Development of sulfide calibration standards for laser ablation inductively-coupled mass spectrometry technique. J Anal At Spectrom 17:406–409

Zientek ML (2012) Magmatic ore deposits in layered intrusions - Descriptive model for reef-type PGE and contact-type Cu–Ni–PGE deposits. U.S. Geological Survey Open File, http://pubs.usgs.gov/of/2012/1010/contents/OF12-1010.pdf